Research Square

Preprints are preliminary reports that have not undergone peer review.
They should not be considered conclusive, used to inform clinical practice,
or referenced by the media as validated information.

Dynamic cortical responses to premature contractions of the heart in humans

Pia Reinfeld

reinfeld@cbs.mpg.de

Max-Planck Institut for Human Cognitive and Brain Sciences https://orcid.org/0000-0001-8644-2229

Eva Greschke

Max-Planck Institut for Human Cognitive and Brain Sciences

Tim Paul Steinfath

Max Planck Institute for Human Cognitive and Brain Sciences https://orcid.org/0000-0002-7388-9870

Pei-Hsin Ku

National Yang Ming Chiao Tung University

Hannah Frome

University Hospital Leipzig

Tobias Uhe

University Hospital Leipzig

Ulrich Laufs

University Leipzig https://orcid.org/0000-0003-2620-9323

Vadim Nikulin

Department of Neurology, Max Planck Institute for Human Cognitive and Brain Sciences, Leipzig, Germany

Jane Neumann

University of Applied Sciences Jena

Arno Villringer

Max Planck Institute for Human Cognitive and Brain Sciences https://orcid.org/0000-0003-2604-2404

Article

Keywords:

Posted Date: August 22nd, 2026

DOI: https://doi.org/10.21203/rs.3.rs-10703389/v1

License: This work is licensed under a Creative Commons Attribution 4.0 International License.
Read Full License

Additional Declarations: There is **NO** Competing Interest.

Dynamic cortical responses to premature contractions of the heart in humans

Pia Reinfeld[1,2,3*], Eva Greschke[1*], Tim Paul Steinfath[1,4], Pei-Hsin Ku[5,6], Hannah Shirin Frome[7], Tobias Uhe[7], Ulrich Laufs[7], Vadim Nikulin[1], Jane Neumann[1,2], Arno Villringer[1,8,9*]

[1]Department of Neurology, Max Planck Institute for Human Cognitive and Brain Sciences, Stephanstraße 1A, 04103 Leipzig, Saxony, Germany
[2]Department of Medical Engineering and Biotechnology, University of Applied Sciences Jena, Carl-Zeiss-Promenade 2, 07745 Jena, Thuringia, Germany
[3]International Max Planck Research School on Cognitive NeuroImaging, Stephanstraße 1A, 04103 Leipzig, Saxony, Germany
[4]International Max Planck Research School on Neuroscience of Communication, Stephanstraße 1A, 04103 Leipzig, Saxony, Germany
[5]Department of Physical Therapy and Assistive Technology, National Yang Ming Chiao Tung University, No. 155, Sec. 2, Linong St., Beitou Dist., Taipei 112304, Taiwan
[6]Ignite Physio Clinic, No. 888, Sec. 1, Youguan Rd., Luzhu Dist., Taoyuan 338011, Taiwan
[7]Department of Cardiology, University Hospital Leipzig, Liebigstraße 16, 04103 Leipzig, Saxony, Germany
[8]Clinic for Cognitive Neurology, University Hospital Leipzig, Liebigstraße 16, 04103 Leipzig, Saxony, Germany
[9]LIFE-Leipzig Research Center for Civilization Diseases, University Hospital Leipzig, Philipp-Rosenthal-Straße 27, 04103 Leipzig, Saxony, Germany

[*]Corresponding authors: reinfeld@cbs.mpg.de (P.R.); greschke@cbs.mpg.de (E.G.); villringer@cbs.mpg.de (A.V.)

Abstract

Premature contractions (PCs), often perceived as transient stuttering of the heartbeat, are the most common arrhythmias and, when frequent, are associated with adverse cardiovascular outcomes. The neural response to PCs remains unclear, particularly whether it is confined to brainstem reflexes or also engages cortical systems involved in interoception. We studied 103 individuals with frequent PCs (51 atrial, 52 ventricular) and matched controls using simultaneous electrocardiography and electroencephalography; an additional 11 individuals with frequent PCs underwent concurrent functional magnetic resonance imaging with electrocardiography. PCs, especially ventricular PCs, were associated with reduced activity in the insular cortex and anterior cingulate cortex (ACC). The subsequent heartbeat elicited early increases in orbitofrontal and ACC

activity. These findings reveal temporally structured cortical responses to PCs: reduced activity during PCs is compatible with diminished afferent cardiovascular signalling, whereas post-PC activity suggests rapid updating of internal representations following transient disruption of cardiac input.

1 Introduction

Heart rate and blood pressure are dynamically regulated to meet fluctuating physiological and environmental demands, preserving homeostasis across states of activity, emotion, and stress. At the core of this cardiovascular regulation lies the central autonomic network (CAN), which includes the insular cortex, anterior cingulate cortex (ACC), and the amygdala, and relays signals to the cardiovascular system via the thalamus, hypothalamus, and brainstem. The insular cortex is widely regarded as a principal hub for interoceptive processing, integrating afferent visceral signals, including cardiac input [1]. The ACC contributes to the affective evaluation of bodily signals and, within predictive coding frameworks, to the generation and updating of internal models of bodily state [2]. Notably, in mice, the ACC has been shown to be central to heart rate regulation [3]. Together, these regions are thought to maintain dynamic neural representations of cardiovascular activity, forming a foundation for the perception and regulation of internal bodily states and their adjustment to different conditions.

Despite existing theoretical frameworks and animal data, the neural mechanisms underlying cardiovascular adjustments and the roles of different brain areas in humans remain poorly understood. From a predictive coding perspective, the heartbeat is a highly regular signal that enables the brain to predict upcoming cardiac events. A typical experimental design for investigating such systems involves inducing "deviations" and evaluating the brain's response. Experimental perturbation of cardiac rhythm, however, is invasive and ethically constrained in healthy humans. We therefore leveraged naturally occurring premature contractions as intrinsic perturbations of a highly predictable physiological signal.

Premature contractions (PCs), also known as extrasystoles, are the most common arrhythmia, as widely described in healthy populations [4, 5]. They arise from premature depolarisation in the atria (premature atrial contractions, PACs) or ventricles (premature ventricular contractions, PVCs), leading to a contraction earlier than the next expected sinus beat. They can occur in isolation or in clusters. Critically, a PC perturbs more than a single beat: the premature contraction ejects a reduced stroke volume and is followed by a pause and a postextrasystolic beat with elevated stroke volume and contractility [22, 16]; this postextrasystolic beat is further thought to be the one perceived as a palpitation [28]. Despite the high prevalence and clinical significance of these at least transient failures of the regular heartbeat, nothing is known about the neural events associated with PCs. Thus, we specifically asked (i) whether transient

cardiac perturbations engage higher-order CAN regions, (ii) whether the heartbeat immediately following a PC recruits distinct neural mechanisms associated with updating internal bodily representations, and (iii) whether frequent PCs are associated with altered processing of regular sinus beats.

To address these questions, we identified 103 individuals with frequent PCs (at least 25 PCs within a 20 min recording) from a database of 3492 simultaneous ECG-EEG recordings of a population-based study [6]. Taking advantage of EEG's high temporal resolution, we differentially assessed cortical responses to PCs and the immediately following heartbeats. In addition, we performed a combined ECG-fMRI study in 11 individuals with frequent PCs to take advantage of MR's high spatial resolution. Combining EEG and fMRI enabled complementary characterisation of temporal and spatial neural dynamics following cardiac perturbations.

2 Results

2.1 EEG analysis

We analysed the temporal dynamics of PCs in brain activity by examining the EEG time-locked to the R-peak in the ECG (heartbeat-evoked potential, HEP, as first described by Schandry et al. [7]). Specifically, we compared the cortical response to the PC and the subsequent beat (PC+1) with the response to the regular (sinus) reference beat (PC-3), i.e. the beat occurring three beats before the PC (see Section 4.1.5).

Comparing all PCs to the reference beats, we identified a significantly smaller HEP in both negative and positive clusters within the 250 ms to 330 ms time window. The negative cluster was identified over central-occipital electrodes (Monte Carlo $p < 0.0362$). The positive cluster was located over central-frontal electrodes (Monte Carlo $p < 0.0006$). PVCs and PACs were retested individually to determine whether either type of PC primarily drove the results. While no significant differences were found between PACs only and the reference condition ($p > 0.05$, Supplementary Fig. 2), statistical tests revealed a significant difference between the PVC condition and the reference, similar to the effect observed in the PC condition. Thus, the effects observed for all PCs were primarily driven by PVCs. The comparison between PVCs and the reference condition revealed one negative and one positive cluster from 220 ms to 350 ms. The negative cluster was located over central-occipital electrodes (Monte Carlo $p < 0.0008$), whereas the positive cluster was found over central-frontal electrodes (Monte Carlo $p < 0.0002$, Fig. 1).

We further determined whether the evoked brain activity following the heartbeat immediately after the premature contraction (PC+1) differed from the reference condition (PC-3). The analysis revealed a significant difference between the conditions corresponding to one positive and one negative cluster in the observed data from 130 ms to 200 ms (both Monte Carlo $p < 0.0002$). The negative cluster was distributed over central-frontal and the positive cluster over central-

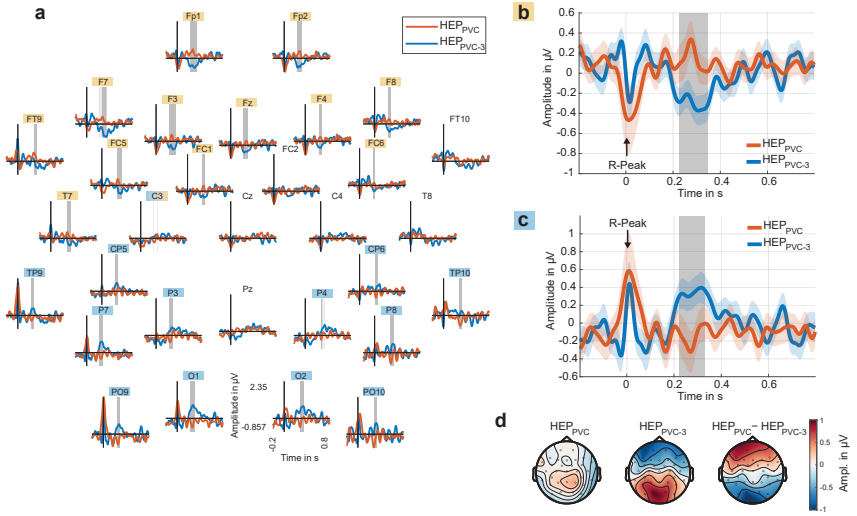


Fig. 1: Premature ventricular contractions are associated with reduced neural activity. HEP of PVC and reference condition (PVC-3). Grand average over all PVC participants ($N = 52$). **(a)** HEPs in each EEG channel. **(b)** Positive cluster averaged over central-frontal electrodes (Monte Carlo $p < 0.0002$) between the PVC and reference conditions. Electrodes used for averaging are highlighted in orange. The grey-shaded area highlights the time window of the found cluster. The colour-shaded regions around the lines mark the ±1 SEM (standard error of mean). **(c)** Negative cluster averaged over central-occipital electrodes (Monte Carlo $p < 0.0008$) between the PVC and reference conditions. Electrodes used for averaging are highlighted in blue. The grey-shaded area highlights the time window of the found cluster. The colour-shaded regions around the lines mark the ±1 SEM. **(d)** Topographies of HEPs in PVC, PVC-3 and difference between conditions between 220 ms and 350 ms after R-peaks.

occipital electrodes. Most notably, the HEP appeared earlier and with increased amplitude in the PC+1 condition than in the reference condition (Fig. 2).

Separate analyses of the two types of PCs revealed a significant difference between PVC+1 and the reference condition (PVC-3), manifested in a positive and negative cluster from 140 ms to 210 ms. The negative cluster was identified over the central-frontal electrodes (Monte Carlo $p < 0.0004$), whereas the positive cluster was observed over central-occipital electrodes (Monte Carlo $p < 0.0004$).

A similar effect was found when comparing PAC+1 with the reference (PAC-3). Statistically significant negative and positive clusters were detected from 120 ms to 180 ms. The negative cluster appeared in the central-frontal electrode region (Monte Carlo $p < 0.0002$) and the positive cluster was located in the

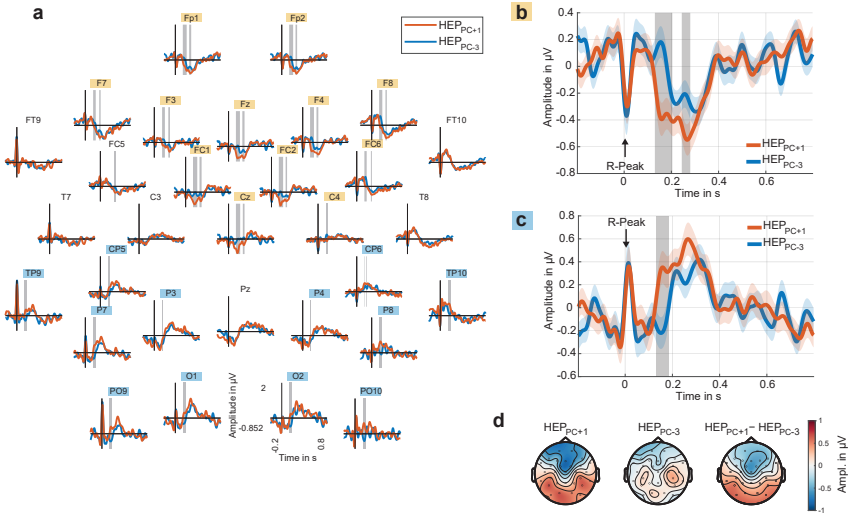


Fig. 2: The first postextrasystolic beat evokes earlier and larger neural activity. HEP of PC+1 and reference condition (PC-3). Grand average over all participants ($N = 103$). **(a)** HEPs in each EEG channel. **(b)** Negative cluster averaged over central-frontal electrodes (Monte Carlo $p < 0.0002$) between the PC+1 and reference conditions. Electrodes used for averaging are highlighted in orange. The grey-shaded area highlights the time window of the found cluster. The colour-shaded regions around the lines mark the ±1 SEM. **(c)** Positive cluster averaged over central-occipital electrodes (Monte Carlo $p < 0.0002$) between the PC+1 and reference conditions. Electrodes used for averaging are highlighted in blue. The grey-shaded area highlights the time window of the found cluster. The colour-shaded regions around the lines mark the ±1 SEM. **(d)** Topographies of HEPs in PC+1, PC-3 and difference between conditions between 130 ms and 200 ms after R-peaks.

central-occipital region (Monte Carlo $p < 0.0013$).

Because similar temporal and topographic effects were observed for both the PVC+1 and PAC+1 conditions, we then determined the extent of their similarity. For this purpose, we statistically compared PVC+1 and PAC+1 over the entire period. No significant difference was found between the two PC groups ($p > 0.05$, Supplementary Fig. 3). Therefore, to increase the sample size and improve the signal-to-noise ratio for subsequent analysis steps, they were combined into a single condition (PC+1).

To assess the robustness of the effects, we repeated our analysis with varying preprocessing parameters in a multiverse analysis. Most notably, the conditions PVC, PC+1, PAC+1, and PVC+1 remained significantly different from the reference condition, with similar cluster characteristics (Supplementary Table 1), highlighting that the results are not sensitive to preprocessing options.

2.2 Source-space analysis

Source reconstruction of the EEG data using eLORETA was applied to the averaged HEP within the time windows that exhibited the most pronounced differences and the resulting sources of the conditions (PVC, PC+1) were compared with those of the reference condition.

The reconstruction revealed a primary difference in the HEP source amplitude between PVC and the reference condition in the left insula ($p_{\mathrm{FDR}} < 0.047$, Supplementary Table 2, Fig. 3), significant across all six multiverse pipelines. Whether this reflected greater or smaller activity for PVC relative to the reference condition, however, depended on the regularisation parameter of the source reconstruction, which trades off spatial precision against noise robustness. Activity was greater for PVC at the highest value (0.5) and smaller at the two lower values (0.05, 0.001), irrespective of the aggregation method used to combine dipoles into the region of interest (ROI) (Supplementary Table 2). This pattern is consistent with how regularisation affects deep sources such as the insula: high regularisation values filter out their already attenuated signal and leave the estimate dominated by leakage from stronger, more superficial neighbours, whereas lower regularisation better recovers the local source at the cost of greater noise sensitivity.

Additionally, the left postcentral gyrus reached significance in five of the six pipelines ($p_{\mathrm{FDR}} < 0.044$), consistently in the same direction across all six, including the pipeline that did not reach significance, making it a strong candidate for a genuine effect. The right postcentral gyrus, left and right orbitofrontal cortex (OFC), and right ACC each reached significance in up to three of the six pipelines. As our criterion for highlighting a primary finding required significance across all six pipelines, we did not focus on these sources further. This strict criterion may, however, have rejected relevant sources, which is why we additionally examined all regions in the fMRI results.

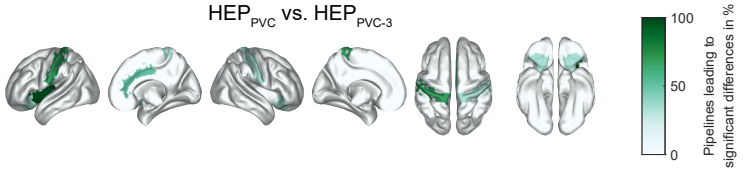


Fig. 3: The PVC-evoked neural difference localises mainly to the left insula across the multiverse analysis. Multiverse source-space analysis of HEPs of PVC vs PVC-3 in the 220 ms to 350 ms time window. Each ROI is colour-coded to indicate the number of multiverse pipelines with a significant difference between conditions, relative to the total number of pipelines (6).

Significant differences in the HEP amplitude between the PC+1 and reference conditions (PC-3) in source-space were observed in the left OFC and both the left and right ACC ($p_{\mathrm{FDR}} < 0.035$, Supplementary Table 3, Fig. 4), significant across all six pipelines and consistently in the same direction. The right

OFC was significant in five of the six pipelines ($p_{\mathrm{FDR}} < 0.048$) and, like the left OFC and ACC, consistently in the same direction across all six, including the pipeline that did not reach significance, again a strong candidate for a genuine effect. The right insular cortex was also significant in five of the six pipelines, but, as in the left insula in the PVC condition above, its direction reversed with regularisation, again attributable to leakage rather than a genuine reversal of the underlying effect. The left and right postcentral gyri each reached significance in up to three of the six pipelines, specifically the three using sign-flip correction (AVG-SF), likely reflecting cancellation of oppositely oriented dipoles under naive averaging. As above, we did not focus on these sources further given our all-pipeline criterion, and further conducted the fMRI study for the same reason.

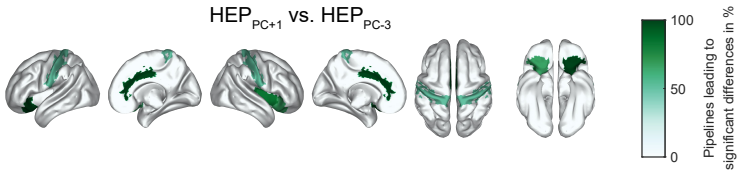


Fig. 4: The PC+1-evoked neural difference localises mainly to OFC and the ACC across the multiverse analysis. Multiverse source-space analysis of HEPs of PC+1 vs PC-3 in the 130 ms to 200 ms time window. Each ROI is colour-coded to indicate the number of multiverse pipelines with a significant difference between conditions, relative to the total number of pipelines (6).

To determine whether the premature and more pronounced HEP at PC+1 reflects scaled-up activity originating in typical HEP sources or additional activity within a distinct source configuration, the PC+1 sources were compared with the temporal development (130 ms to 620 ms) of source activation for the HEP in the reference condition with the same multiverse analysis. Most notably, the left and right ACC were significantly more active in the PC+1 condition across 30 of 42 pipelines (7 time windows × 3 regularisation parameters × 2 aggregation methods, $p_{\mathrm{FDR}} < 0.05$, Supplementary Fig. 4), indicating a distinct source configuration for the observed neural response at PC+1.

2.3 Control analysis

To ensure that the main EEG findings are robust to cardiac field artefacts (CFA, [8, 9, 10, 11]) and other fluctuations in cardiac parameters, we conducted several control analyses. We ensured that the differing morphology of the PVC did not influence our results (Supplementary information A.1), compared the ECG signals of the PC+1/PVC condition with the reference condition (Supplementary information A.2), correlated the ECG with EEG (Supplementary information A.3) and repeated the EEG analyses after matching T-wave amplitudes (Supplementary information A.4). The results suggest that the observed

differences in the HEP of PVC and PC+1 were independent of variations in cardiac parameters.

2.4 Comparison to matched control group

To assess whether the HEPs of sinus beats are generally altered in participants who frequently experience premature contractions, we compared the HEPs of regular (during sinus rhythm) heartbeats from participants in the PC group with those from participants without PCs. We found no significant difference between the PAC group and their matched controls. The PVC group showed a significant difference, characterised by a small cluster over the left frontal electrodes ($p < 0.03$), as described in the Supplementary information A.5.

2.5 fMRI analysis

11 participants (mean age: 54.1 ± 16.2 years, range $[37, 79]$; 5 females, 6 males) met all eligibility criteria and exhibited PCs during MRI scanning, yielding usable resting-state fMRI data; individual characteristics are summarised in Table 1.

Table 1: Characteristics of the 11 fMRI participants. Scan PC count is reported as mean ± SD [range]; PC subtype as counts; PVC and PAC 24-hour Holter counts as median [IQR], given the strongly skewed distributions (PVCs range $[0, 19908]$; PACs range $[7, 7365]$). IQR: interquartile range.

ID	PC subtype	PCs (fMRI-session)	PVCs (24h-Holter)	PACs (24h-Holter)
sub-03	PVC	102	14,392	183
sub-07	PAC	85	796	7365
sub-09	PVC	51	19,908	9
sub-10	PVC	7	992	7
sub-13	PVC	54	15,257	516
sub-16	PVC	119	7564	8
sub-17	PVC	10	459	8
sub-23	PAC	47	21	4880
sub-31	mixed	18	2437	2355
sub-33	PAC	37	0	1109
sub-35	PVC	6	7480	63
mean ± SD [range]; median [IQR]	7 PVC, 3 PAC, 1 mixed	48.7 ± 39.1 $[6, 119]$	2437 $[628, 10978]$	183 $[8, 1732]$

We compared the PC-evoked blood-oxygenation-level-dependent (BOLD) signal with the BOLD signal evoked by a reference condition consisting of regular heartbeats during sinus rhythm. Using non-parametric permutation test-

ing (randomise/threshold-free cluster enhancement score (TFCE)), we identified nine significant clusters of BOLD signal decrease ($p < 0.05$, family-wise error (FWE) corrected).

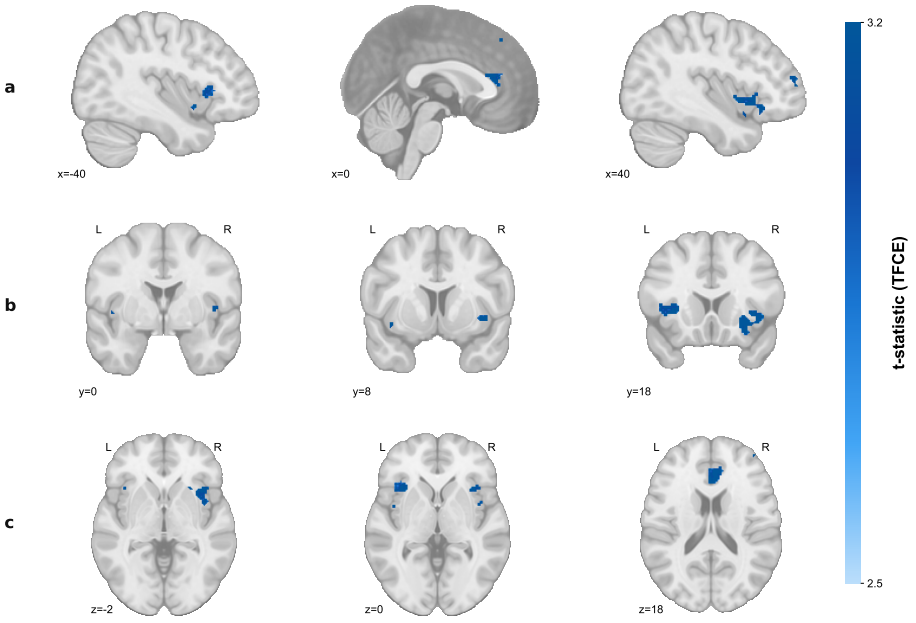


Fig. 5: Premature contractions evoke bilateral insular-ACC deactivation. Whole-brain BOLD signal decreases in response to PCs relative to regular heartbeats (during sinus rhythm) (randomise/TFCE, FWE $p < 0.05$; $N = 11$). Colour scale reflects t-statistic magnitude (TFCE score). Representative sagittal, coronal, and axial slices are shown at cluster centres of gravity on the MNI152 standard brain. L: left; R: right.

The most extensive clusters were centred on the right insular cortex (peak MNI $[38, 10, -18]$; 485 voxels), the left insular cortex including parts of the frontal operculum (peak MNI $[-38, 18, -2]$; 218 voxels), and bilateral ACC (peak MNI $[-2, 32, 8]$; 210 voxels; Fig. 5). Additional smaller clusters appeared again in the left insular cortex (peak $[-38, 4, -12]$ and peak $[-42, 2, 0]$) as well as in the right frontal pole (peak $[42, 54, 8]$), right superior frontal gyrus (peak $[6, 38, 40]$), left supramarginal gyrus (peak $[-50, -40, 42]$), and left Heschl's gyrus (peak $[-44, -16, 8]$). These findings were corroborated by FLAME 1+2 parametric mixed-effects modelling, yielding spatially concordant clusters centred on the same primary regions (Supplementary Table 4). Effect sizes

were large at the primary ROIs (Right Insular Cortex: $d = 1.25$, $p = 0.001$; Left Insular Cortex: $d = 1.44$, $p = 0.0004$; ACC: $d = 1.08$, $p = 0.0025$) and results were consistent across all three statistical frameworks (Supplementary Fig. 5). No significant BOLD signal increases (PCs > reference condition) were detected. Complete cluster statistics are provided in Table 2; the complete cluster statistics of the corroborative analyses are reported in Supplementary Tables 4–5.

Table 2: BOLD signal decreases in response to premature contractions. Randomise/TFCE (FWE $p < 0.05$), full sample ($N = 11$), PCs < regular heartbeats. Clusters are ordered by volume. MNI coordinates refer to MNI152 standard space (2 mm isotropic). TFCE: threshold-free cluster enhancement score (randomise). p: family-wise error (FWE)-corrected cluster p-value. Anatomical labels from the Harvard-Oxford Cortical and Subcortical Structural Atlases (2 mm maximum probability atlas, 25 % threshold; regions with ≥5 % probabilistic overlap reported). ACC: anterior cingulate cortex; COG: centre of gravity; HO: Harvard-Oxford; L: left; R: right; post.: posterior division.

Cluster	Voxels	Peak MNI (x, y, z)	p	Peak region (HO atlas)	COG region (HO atlas)
1	485	38, 10, −18	0.0444	R Insular Cortex	R Insular Cortex
2	218	−38, 18, −2	0.0439	L Insular Cortex	L Insular Cortex/Frontal Operculum
3	210	−2, 32, 8	0.0444	L/R ACC	R ACC
4	79	42, 54, 8	0.0474	R Frontal Pole	R Frontal Pole
5	34	6, 38, 40	0.0464	R Superior Frontal Gyrus/Paracingulate Gyrus	R Superior Frontal Gyrus
6	16	−38, 4, −12	0.0464	L Insular Cortex	L Insular Cortex
7	13	−50, −40, 42	0.0464	L Supramarginal Gyrus (post.)	L Supramarginal Gyrus (ant.)
8	5	−42, 2, 0	0.0483	L Insular Cortex	L Insular Cortex
9	5	−44, −16, 8	0.0498	L Heschl's Gyrus	L Heschl's Gyrus/Central Opercular Cortex

3 Discussion

During premature contractions (PCs), predominantly premature ventricular contractions (PVCs), EEG and fMRI recordings show reduced cortical activity in regions of the central autonomic network (CAN), most consistently in the insula and the anterior cingulate cortex (ACC). Subsequently, during the first post-PC heartbeat, earlier and stronger evoked activity was observed in the orbitofrontal cortex (OFC) and ACC. These findings suggest that the CAN dynamically responds to premature contractions: the early reduction in activity is consistent with diminished baroreceptor input, while the post-PC activity seems to be consistent with prediction-error signalling and visceromotor adjustment.

Participants with frequent PVCs exhibited different neural activity associated with regular (sinus rhythm) heartbeats compared to a matched control group without PVCs.

The insular cortex emerged as the most consistently and strongly deactivated region across all analyses, with convergent evidence from both examination modalities: fMRI revealed bilateral insular deactivation, and EEG source reconstruction independently localised the dominant effect to the left insular cortex. This multimodal convergence strengthens confidence in the insular cortex as a primary site of altered neural processing during PCs. The insular cortex occupies a central role in interoceptive processing, the neural representation of the body's internal physiological state, and has been consistently implicated in cardiac signal detection and the conscious awareness of heartbeats [14, 15, 1]. The deactivation of the insula relative to regular heartbeats most parsimoniously reflects reduced baroreceptor afferent input during the PC cycle: compared to a regular sinus beat, the attenuated stroke volume and compensatory post-ectopic pause substantially reduce the cardiac afferent signal reaching the insular cortex [16, 17, 18]. Disentangling this account from complementary predictive coding interpretations will be addressed below.

EEG showed a clear predominance of the effect in the insula for PVCs vs premature atrial contractions (PACs). Whereas PVCs were associated with a robust and spatially consistent reduction in evoked brain activity over central-frontal and central-occipital electrode clusters, no significant effect was detected for PACs alone. This dissociation is neurophysiologically plausible: PVCs produce more pronounced hemodynamic perturbations than PACs, including greater reductions in stroke volume, more marked pulse deficits, and a longer compensatory pause [16, 17]. The stronger hemodynamic deviation associated with PVCs would therefore be expected to generate a larger reduction in baroreceptor afferent input and thus a larger difference in the cortical response. Consistent with this interpretation, the fMRI data showed higher peak Z-statistics in the PVC-dominant subgroup (Supplementary Fig. 6). This is compatible with reduced between-subject heterogeneity when the sample is restricted to a single, dominant PC subtype, since pooling PVCs and PACs, which likely differ in the magnitude of their hemodynamic effects, may attenuate the group-level effect; formal inference nonetheless remains limited at $N = 7$.

The ACC co-deactivated with the insular cortex across all fMRI analyses and also in some EEG analyses. It is a key node in the CAN and has been consistently implicated in integrating interoceptive signals with higher-order cognitive and affective processing [19, 20]. Analogous to the mechanism proposed for the insular cortex, ACC deactivation during PCs most parsimoniously reflects reduced cardiovascular afferent input during the PC cycle. The relatively lower effect size at the ACC in the fMRI ($d = 1.08$) compared to the insular cortex ($d = 1.25$–1.44) and less consistent EEG deactivation may, however, point to an additional opposing process: a transient activity rebound that partially offsets the deactivation; in the fMRI, the hemodynamic response function underlying the BOLD signal prevents a clear separation of two subsequent heartbeats, whereas in the EEG, the two subsequent heartbeats can be temporally resolved

allowing identification of a rebound of activity in the ACC in the first beat after the PC following the compensatory pause [16, 17].

Untangling the temporal dynamics of neural responses, we found that activity associated with the first postextrasystolic heartbeat originated from distributed cortical sources, predominantly in the OFC and ACC. This manifested as an early and increased evoked neural response in the first postextrasystolic heartbeat, primarily in the 130 ms to 200 ms time window, a period during which we did not observe evoked brain activity with regular heartbeats. It might be argued that postextrasystolic potentiation, i.e., increased blood pressure, stroke volume, and contractility during the beat following a premature contraction, directly influences the amplitude of heartbeat-evoked neural responses via increased firing of baroreceptors, cardiac neurons, or somatosensory pathways [21, 22, 23]. Moreover, intracranial studies have demonstrated that a neural response to the heartbeat is detectable as early as 100 ms after the R-peak [24, 25]. However, while these direct influences on evoked brain activity via fast pathways align with the earlier timing of the neural response observed in the study, our source analysis suggests an additional mechanism. If the early difference in evoked activity were solely due to a stronger and earlier cardiac signal, we would expect to observe overall stronger activity in typical HEP sources during this earlier time window. However, we identified a distinct source almost exclusively active during this early time window in postextrasystolic heartbeats. The ACC was neither as active in the same early time window as in the reference condition (during sinus rhythm) nor at the time of the highest amplitude, or at any other time window during the evoked response to the reference condition. This indicates that a mere scaling of normal (related to sinus rhythm) heartbeat-evoked activity, due to potentially stronger afferent activity, cannot fully explain the neural alterations associated with the first postextrasystolic beat.

Therefore, an additional neural mechanism may underlie the distinct source configuration in this early window, possibly aligning with predictive accounts of interoception. The brain uses prior heartbeats to anticipate the regular rhythm and strength of upcoming beats [26]. A PC disrupts this regular pattern, leading to unmet predictions, especially during PVCs. During the long compensatory pause after a PC, sympathetic activity continues to rise rather than being inhibited, potentially heightening anticipatory processing [27]. Because maintaining a regular heartbeat is vital, deviations beyond normal variability may signal internal threats and prompt visceromotor adjustments, such as heart rate turbulence after PCs. Further, PCs often result in heightened sensation in the following beat [28], clinically observed as palpitations, potentially reflecting this mismatch between expectation and sensation. Importantly, the neural sources related to the first postextrasystolic beat, i.e., the ACC, are known to be implicated in processing deviations between anticipated cardiovascular parameters and actual sensory input [29, 26, 30, 31].

Previous studies have reported changes in HEP linked to predictive processing across sensory modalities. For example, Pfeiffer and De Lucia found that unexpected omissions in auditory sequences synchronised to the heartbeat

elicited a slightly earlier and larger HEP amplitude, suggesting the brain integrates interoceptive signals when processing regularity [29]. Banellis and Cruse found similar effects modulated by attention and synchronicity within an early HEP window that overlaps with our study [30]. Our results align with these in both timing and concept, as the irregular rhythm of a premature contraction likely elicits a surprise response within a similar time frame [32]. Notably, in contrast to the earlier studies, here we show mismatch-like responses to purely interoceptive cardiac events.

While we restricted EEG source reconstruction to established, hypothesis-driven a priori interoceptive ROIs (following Kumral et al. [33]) to stabilise the ill-posed inverse solution, we applied a whole-brain approach in fMRI, with its high spatial specificity, to survey effects without regional constraints, thereby revealing additional brain areas with significant effects. Beyond the primary insular-ACC deactivation pattern, the fMRI analyses revealed additional deactivations in the bilateral supramarginal gyri and in frontal and lateral occipital regions. Of these, the supramarginal gyrus deactivation was the most spatially consistent, replicating across all three statistical frameworks, bilaterally in the FLAME analyses and in the left hemisphere under non-parametric testing. The supramarginal gyrus is implicated in integrating interoceptive and exteroceptive bodily signals and has been identified as a primary convergence zone for interoceptive and body-ownership-related processing in neuroimaging meta-analyses [34]. Its deactivation during PCs may reflect a transient disengagement from ongoing multisensory bodily self-monitoring, consistent with the broader reorganisation of interoceptive processing proposed above. Frontal and lateral occipital deactivations were less spatially consistent and are therefore not interpreted in detail here; their potential role in attentional modulation during anomalous cardiac events awaits replication in larger samples.

Alongside these cortical findings, a deactivation cluster was also observed at the subcortical level. The peak coordinate of the brainstem cluster (MNI $[8, -28, -36]$) is anatomically consistent with the dorsal medulla, encompassing the nucleus tractus solitarius (NTS), the primary central relay for cardiovascular afferent signals, and the dorsal motor nucleus of the vagus nerve [35]. Brainstem deactivation during PCs may reflect the transient reduction in baroreceptor afferent input to the NTS during the compensatory post-PC hemodynamic response, directly analogous to the mechanism proposed for the insular deactivation. This finding should be interpreted with caution, however: the brainstem cluster did not survive non-parametric permutation testing or the most conservative FLAME 1 analysis, and the standard EPI sequences employed here are not optimised for brainstem imaging. Dedicated brainstem-optimised sequences would be required for definitive characterisation.

Participants with frequent PVCs but not PACs differed in their heartbeat-evoked brain activity time-locked to normal sinus-rhythm heartbeats compared with a matched control group without premature contractions in the EEG analysis. For this comparison we found a significant difference in the left frontal electrodes. Higher amplitudes in the left frontal HEP may indicate altered heart-brain interaction due to a compensatory upregulation of heartbeat sen-

sitivity, driven by frequent transient heart failures. In contrast, we did not observe a significant effect in the PAC comparison, possibly because PACs have lower hemodynamic impact and may therefore appear less symptomatic than PVCs [16, 17].

From a methodological perspective, we employed two neuroimaging methods: EEG and fMRI, which rely on different physical and physiological signals. Methodological scrutiny is crucial for the validity of the findings for both methods. In the EEG, the neural response, time-locked to the R- or T-peaks of the ECG, is detectable as early as 100 ms after the R-peak in regions such as the insula, ACC, and somatosensory cortex, consistent with findings from intracranial studies [21, 24, 25]. However, the noninvasive assessment of these signals in the EEG requires careful attention to the methodology and interpretation to ensure accurate results, as we recently reviewed [36]. Therefore, we employed a multiverse pipeline for time domain and source analyses to ensure robust results across different parameter settings, as described in Sections 4.1.5 and 4.1.7. Furthermore, multiple control analyses were conducted to rule out the possibility that our findings were attributable to cardiac field artefacts. We used within-participant comparisons, independent component analysis (ICA) cleaning, polarity grouping for the PVC analysis, and correlation analyses to minimise and control for artefactual effects (see Section 4 and Supplementary information A.3). Nevertheless, incorporating additional ECG channels could enhance the control of cardiac artefacts, as different ECG electrodes may capture varying parts of the artefact, depending on their placement [37]. Another limiting factor in our study is the relatively short recording time of only 20 minutes. After preprocessing, this resulted in approximately 30 epochs/valid premature contractions per participant, whereas HEPs are typically averaged over 70 to 1600 epochs [38]. It is all the more remarkable that, despite this limitation, significant differences in the HEPs for PVC and PC+1 were found.

Regarding the fMRI findings, the sample size of 11 might appear small, however, several methodological aspects strengthen confidence in the results. The use of three inferential approaches with distinct statistical assumptions provides convergent validation, and the explicit modelling of regular heartbeat onsets as a reference regressor ensures that artefactual signals common to all heartbeats are controlled for by subtraction, while PC-specific neural responses remain detectable as the contrast of interest. The within-subject design, with PC-evoked responses estimated from naturally occurring events (48.7 ± 39.1 PCs; range: $[6, 119]$), provides considerably greater statistical leverage than a between-group comparison of equivalent size. Limitations include the inability to classify individual PC events as PVC or PAC during scanning due to MRI gradient artefacts, the inability to model the post-PC beat separately given BOLD temporal resolution constraints, and the naturalistic resting-state paradigm which limits causal inference. Future studies leveraging sub-second whole-brain fMRI acquisition [39, 40] may better resolve the temporal dynamics of cardiac event-related responses.

The present findings reveal that premature cardiac contractions engage the insular cortex and ACC—key nodes of the CAN implicated in interoceptive pro-

cessing and autonomic regulation. Converging evidence across fMRI and EEG indicates reduced insular activity during PCs, alongside a temporally evolving ACC response characterised by deactivation during the PC and postextrasystolic rebound activity. Together, these findings identify the CAN as an active participant in the cortical processing of cardiac irregularities, extending beyond brainstem reflexes to engage higher-order interoceptive and predictive circuits.

Given that these regions are also implicated in emotional processing and conscious access to bodily signals, future studies could examine whether individual differences in neural responses to premature contractions contribute to variability in emotional reactions and conscious perception of them. More broadly, characterising cortical responses to cardiac irregularities may provide insight into the high psychological comorbidity associated with frequent PCs, including anxiety and depression, and may help clarify emerging links between cardiac arrhythmias, cognitive decline, and dementia risk.

4 Methods

4.1 EEG analysis

4.1.1 Participants

Participants were selected from the population-based study of the Leipzig Research Center for Civilization Diseases (LIFE-Adult) [6]. Initially, we selected 3492 participants who had simultaneously recorded ECG and resting-state EEG. Out of 2228 participants who displayed at least one PAC or PVC beat, 103 participants meeting the criteria were enrolled for analysis, including 51 for the PAC condition and 52 for the PVC condition (Supplementary Fig. 7); one person displayed both types and is therefore represented in both groups. We only included participants with at least 25 isolated PAC or PVC beats. To minimise the influence of other cardiac impairments, participants with more than five detected PAC/PVC trigeminy, bigeminy, runs, couplets, one or more prolonged R-R intervals, pacemakers, tachycardia, bradycardia, atrial fibrillation, or atrial flutter were excluded from the study. The CER-S (Continuous ECG Recording Suite) software developed by AMPS (Analysing Medical Parameters for Solutions) automatically detected all the ECG patterns. CER-S is designed for scientific ECG analysis and supports data formats from 1- to 12-channel ECGs and open-standard formats like MIT-WFDB, which was utilised in this study. The software employs the ABILE algorithm to detect and analyse heartbeats in an ECG [41]. The maximum coupling interval for detecting PCs was set to the default value 75 % of the AMPS software. After detection, two researchers manually inspected and finalised the beats as described in Section 4.1.3. The mean age was 70.91 ± 4.51 years for people allocated to the PAC condition (male: 32, female: 19) and 70.76 ± 4.89 years for those in the PVC condition (male: 33, female: 19). Unless stated otherwise, descriptive values are reported as mean $\pm$ SD.

4.1.2 Recordings

The 20 min resting EEG was recorded in an electrically shielded and sound-attenuated booth. 34 passive Ag/AgCl electrodes were used, including 31 scalp electrodes placed according to the 10-20 system on an EEG cap. Additionally, two electrodes captured vertical and horizontal eye movements, while a bipolar electrode on the forearm simultaneously recorded the ECG. The signals were amplified using a QuickAmp amplifier (Brain Products). EEG signals were referenced against the common average and recorded at a sampling rate of 1000 Hz, with a low-pass filter set at 280 Hz. Impedance levels were kept below 10 kΩ.

4.1.3 ECG preprocessing

We analysed all ECGs from participants with ECG and EEG recordings using CER-S, along with custom-written Bash scripts. The number of PCs for both types (PAC and PVC) was extracted to select participants. We visually inspected the detected PCs and regular sinus beats within each selected participant. If necessary, we adjusted the detection trigger, which marked the time point of the R-peak, or excluded participants from the analysis if (1) the researchers were not able to identify a clear P-wave, (2) atrial fibrillation or flutter was present, or (3) the artefacts from the recordings interfered with the identification of cardiac rhythm. Due to the distinct morphology of PVCs compared to regular heartbeats, the highest initial deflection was used as the "R-peak" for PVC detection, as exemplified in Fig. 6.

We then imported the R-peak triggers as events into EEGLAB/FieldTrip. PCs and sinus beats occurring in segments with EEG artefacts were excluded from the analysis. Isolated PCs, those with only sinus beats in the four beats preceding and five following the PC, were labelled accordingly. When the PAC and PVC groups were combined, the events were labelled as "PC" for the premature contraction itself. The additional labels "PC-1", "PC-2", and "PC-3" were used for the beats preceding the premature contraction, and "PC+1" and "PC+2" for the beats following the premature contraction. This labelling scheme was similarly applied to both PAC and PVC (Fig. 6). Regular sinus beats without any temporal relation to the premature contractions were labelled "N".

Among the selected 103 participants, we detected 3202 PCs from 51 participants for the PAC condition and 3345 PCs from 52 for the PVC condition. On average, there were 62.78 ± 50.24 PCs per person for PAC (range $[26, 234]$) and 64.33 ± 47.06 for PVC (range $[25, 238]$). After the ECG preprocessing, 1443 PACs and 1622 PVCs met the criteria and were selected for analysis. This resulted in an average number of PCs per person of 28.29 ± 16.64 for PAC (range $[8, 105]$) and 31.19 ± 15.03 for PVC (range $[9, 77]$).

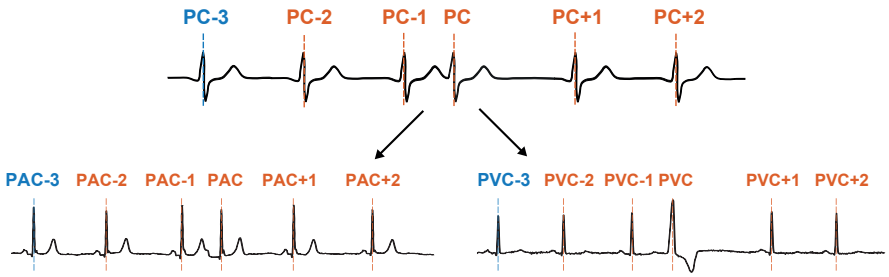


Fig. 6: Beat labelling scheme relative to the premature contraction. Illustration of the different beat types. The top row displays a schematic ECG where both types of PCs are aggregated. Each R-peak is annotated with the beat annotations used in this study. The bottom row shows ECGs derived from actual participant data for PACs and PVCs separately with beat annotations. The reference condition is annotated in blue (see Section 4.1.5).

4.1.4 EEG preprocessing

The EEG was preprocessed using custom scripts and the MATLAB toolboxes EEGLAB and FieldTrip [42, 43]. For time domain analysis, the EEG data were filtered between 0.5 Hz and 20 Hz using a Hamming windowed sinc FIR filter. The filter order for the FIR filter was automatically determined as implemented in the pop_eegfiltnew function from EEGLAB [42]. The data were downsampled to 500 Hz. The ECG events found by CER-S were added to the ECG and EEG signals as event markers. Extended Infomax algorithm-based ICA was applied to the EEG data, which was epoched between −200 ms and 200 ms around the R-peaks and filtered between 1 Hz and 20 Hz to identify and remove artefacts from ocular, muscular, and heartbeat sources. To identify CFAs, the independent component (IC) and ECG time courses were segmented into intervals between −200 ms and 200 ms around the R-peaks and averaged across epochs, as similarly done by Buot et al. [44]. Next, average IC and ECG time courses were correlated, and ICs that correlated with the ECG by more than 0.8 were marked as artefacts and manually inspected before rejection [45, 11]. On average, 1.36 ± 0.86 (range $[0, 4]$) cardiac field components were removed.

4.1.5 HEP analysis

The EEG signals were segmented into epochs between −200 ms and 800 ms around the R-peaks and averaged to analyse the HEP in the time domain. Because a premature beat shortens the interval between the preceding sinus beat (PC-1) and the PC (Supplementary Tables 7 and 8), the tail of the PC-1 heartbeat-evoked response overlaps the early part of the PC epoch; this overlap is absent in the reference condition, whose preceding beat occurs at a normal interval. To prevent this from producing a spurious difference between the PC

and reference conditions, each participant's averaged regular-beat response (N) was subtracted, time-locked to the PC-1 R-peak, from the continuous EEG before the PC epochs were extracted. Baseline correction was performed using the time window from −150 ms to −50 ms before the reference condition PC-3. This ensured that slow fluctuations did not impact the analysed HEP.

Further, different settings were used to test the robustness of the results against variation in the preprocessing pipeline (Fig. 7). Therefore, the analysis was performed without a baseline and with a baseline set immediately before each beat (−150 ms to −50 ms). The HEP analysis was also performed on EEG data that had not been corrected by ICA.

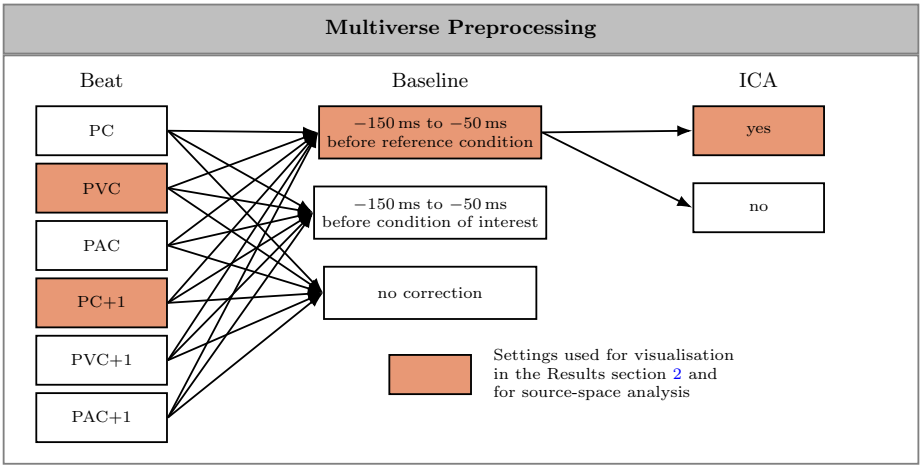


Fig. 7: Multiverse preprocessing pipeline structure. Pipelines of the multiverse preprocessing analyses.

We analysed the grand average HEP for a regular heartbeat (N) of all 103 participants. The HEP appears bipolar, with negative amplitudes in the central-frontal electrodes and positive amplitudes in the central-occipital electrodes (Supplementary Fig. 8).

We used the third beat preceding the PC as a reference condition. We confirmed the choice as suitable by statistically testing whether the beats differed from N in the ECG and EEG. The analysis in the ECG domain showed significant differences between N and the beats PC-2 and PC-1 ($p < 0.05$) but not between PC-3 and N ($p > 0.05$). The cluster-based permutation test, described below, was also performed in the EEG domain between PC-3 and N over the entire time window (−200 ms to 800 ms). This analysis showed no significant difference between the two beats ($p > 0.05$, Supplementary Fig. 9), confirming the suitability of PC-3 as the reference condition. We reconducted the statistical analysis after randomly reducing the number of epochs of the N beat to match the number of PC-3 epochs for an unbiased statistic. Still, there was no significant difference between the two beats ($p > 0.05$). Using PC-3 as the reference guaranteed an equivalent number of beats between the reference condition and

the condition of interest (e.g., PC, PC+1), thereby maintaining a consistent signal-to-noise ratio. It also ensured that spontaneous brain activity occurring around the time of the PC was equally represented in both conditions, thereby preventing it from influencing the result. Further, the within-participant approach helps mitigate the impact of cardiac artefacts, as the stereotypical patterns of these artefacts across heartbeats should cancel each other out during the comparison.

The HEPs of the preceding beats PC-2 and PC-1 did not significantly differ from the reference condition PC-3 ($p > 0.05$, Supplementary Figs. 10 and 11).

No significant difference was observed between PC+2 (PAC+2, PVC+2) and the reference condition PC-3 ($p > 0.05$), suggesting a return to regular brain activity two beats after the PC (Supplementary Fig. 12).

4.1.6 Statistical analysis

Cluster-based permutation t-tests were used to assess within-participant statistical significance between the conditions using the FieldTrip toolbox [46, 43]. This method involves the clustering of samples whose t-values exceed a threshold (cluster threshold p-value: 0.05 two-sided) based on temporal, spatial (and spectral) adjacency and then calculating the cluster statistics by summing the t-values within each cluster. The Monte Carlo method was used to calculate the probability of significance while dealing with the problem of multiple comparisons by randomly permuting the condition labels 5000 times. Clusters with p-values less than 0.05 (corrected for a two-tailed test) and at least two adjacent electrodes were considered significant. The statistical analysis was performed on all EEG electrodes and the entire time window (-200 ms to 800 ms). Similar temporal cluster-based permutation tests were applied to the corresponding ECG signals and for comparisons between participants.

4.1.7 Source-space analysis

The source analysis was performed participant-wise using the 'New York Head' forward model [47]. This finite element method is based on the ICBM152 anatomical template [48]. The lead field matrix of 5004 source dipoles with fixed orientations perpendicular to the cortical surface was used. After removing channels PO5 and PO6, which were not included in the pre-computed lead field, the lead field was transformed to the common mean reference. To solve the inverse problem, exact low-resolution electromagnetic tomography (eLORETA) [49] was applied using the METH toolbox (Guido Nolte; RRID: SCR_016104) with minor modifications by Haufe and Ewald [50]. The regularisation parameter was varied between 0.001, 0.05, and 0.5 to assess the robustness of the results to parameter variations. Furthermore, standard averaging (AVG) and averaging with sign-flip (AVG-SF) were compared to aggregate the dipole sources into single ROIs, as done by Kapralov et al. [51]: AVG-SF reduces the cancellation effect of voxels with opposing dipole orientations within an ROI, an issue that AVG does not account for; as averaging without a sign-flip is

nonetheless also frequently used in practice, we included it to illustrate its effect (see Results). In total, this led to six different pipelines, as illustrated in Fig. 8. This multiverse source analysis was applied at the averaged time window in which the main difference between conditions was observed. To investigate the differences between conditions at the source level, 10 ROIs typically associated with HEP modulations were selected for both hemispheres: posterior cingulate gyrus, ACC, postcentral gyrus, OFC, and insular cortex, similar to Kumral et al. [33]. A dependent t-test was applied to the participant-wise data and corrected for False Discovery Rate (FDR); the resulting significance, direction, and its dependence on the regularisation parameter and aggregation method are reported in the Results (see also Supplementary Tables 2 and 3).

To determine whether the premature and more pronounced HEP at PC+1 originated in typical HEP sources or a distinct source configuration, the PC+1 sources in the time window of 130 ms to 200 ms were compared with sources across individual consecutive time windows of the HEP in the PC-3 condition (7 time windows between 130 ms and 620 ms, width 70 ms). Again, we conducted a dependent t-test for each ROI and all multiverse pipelines to test which sources were significantly more active in the PC+1 condition. However, we broadened our analysis to include all ROIs rather than limiting it to the predefined HEP ROIs.

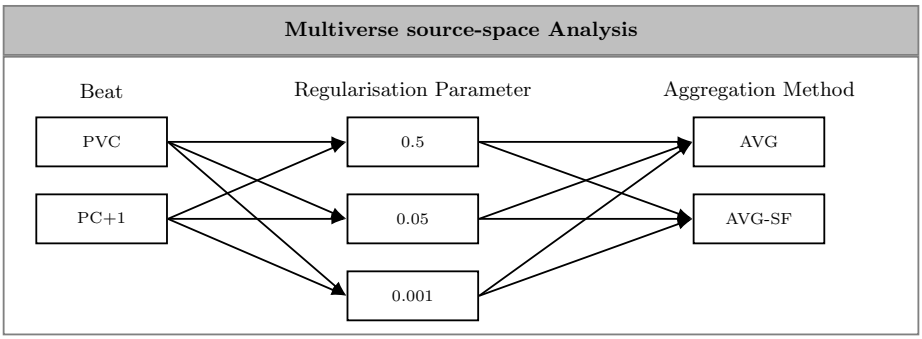


Fig. 8: Multiverse source-space analysis pipeline structure. Pipelines of the multiverse source-space analyses.

4.2 fMRI analysis

4.2.1 Participants

41 native German-speaking adults with documented frequent premature contractions were screened for participation in the fMRI sub-study, of whom two were prospectively designated as pilot participants to evaluate and refine the acquisition workflow and were excluded from all analyses. Inclusion criteria comprised: age $\geq$ 18 years; $\geq$ 450 PCs on 24-hour Holter ECG monitoring; absence of structural heart disease or persistent arrhythmias (confirmed by echocardio-

graphy and 12-lead ECG); absence of neurological or psychiatric comorbidity; no MRI contraindications; and presence of PCs during scanning with sufficient cardiac signal quality (ECG and PPG). 11 of the remaining 39 met all criteria. Participants provided written informed consent before participation. The study was approved by the local ethics committee of the University of Leipzig (280/23-ek) and conducted in accordance with the Declaration of Helsinki.

4.2.2 MRI data acquisition

All MRI data were collected at the Max Planck Institute for Human Cognitive and Brain Sciences (MPI CBS), Leipzig, Germany, using a 3.0 T MAGNETOM Skyra scanner (Siemens Healthineers, Erlangen, Germany) equipped with a 32-channel head coil.

High-resolution T1-weighted anatomical images were recorded using a 3D magnetisation-prepared rapid gradient-echo (MPRAGE) sequence (1 mm isotropic resolution) for structural reference and registration purposes. For resting-state fMRI data acquisition, we used a T2*-weighted multiband gradient-echo echo-planar imaging (EPI) sequence with the following parameters: repetition time (TR) = 1500 ms, echo time (TE) = 30 ms, flip angle = 69°, voxel size = 2.3 mm isotropic, multiband acceleration factor = 4, partial Fourier = 0.875, 64 axial slices, field of view = 202 mm, and bandwidth = 1775 Hz/pixel. A total of 402 volumes were acquired per participant, corresponding to approximately 10 min of continuous scanning. Participants were instructed to keep their eyes open and fixate on a centrally presented cross throughout the full resting-state scan.

To correct for susceptibility-induced geometric distortions, two additional EPI volumes with opposing phase-encoding directions (anterior-posterior and posterior-anterior) were acquired immediately before the resting-state scan and served as the input for B_0 field map estimation. Dummy volumes for T1 equilibration were automatically discarded by the scanner software before data storage. Concurrent ECG and peripheral photoplethysmography (PPG) were recorded throughout scanning using MR-compatible hardware for cardiac event detection and timing verification.

Additional sequences (fMRI task data, 3D T2-weighted SPACE and diffusion-weighted imaging) were acquired but were not utilised in the present analysis (Supplementary information A.6).

4.2.3 Cardiac event detection

Raw ECG data were corrected for MRI gradient and radiofrequency artefacts using custom MATLAB scripts, developed by the Max Planck Research Group Pain Perception, Max Planck Institute for Human Cognitive and Brain Sciences, Leipzig. Premature contractions were subsequently identified by manual annotation of R-peaks by a trained rater who was blind to the neuroimaging data. Simultaneously recorded PPG data were extracted from the DICOM files using the readCMRRPhysio script (CMRR, University of Minnesota; https://github.com/CMRR-C2P/MB) and served as an auxiliary reference for

verifying cardiac timing. Across all 11 participants, a total of 536 PC events were identified (48.7 ± 39.1 per participant; range $[6, 119]$).

Due to substantial residual scanner artefacts, reliable beat-by-beat morphological classification of individual PC events (PVC vs PAC) during the scan was not feasible. PC subtype classification was therefore based on each participant's prior 24-hour Holter ECG (see Section 4.2.7). The post-PC beat was not modelled separately in the fMRI analysis, as the temporal resolution of BOLD imaging relative to the cardiac cycle precludes reliable dissociation of hemodynamic responses to successive beats within a single response window.

4.2.4 fMRI preprocessing

Raw data were organised according to the Brain Imaging Data Structure (BIDS) standard [52] before preprocessing using dcm2niix [53]. Preprocessing was conducted using FSL FEAT (v6.0.7.13), including distortion correction (TOPUP), motion correction (MCFLIRT), slice-timing correction, boundary-based registration (BBR) to the T1-weighted image, nonlinear normalisation to MNI152 standard space (FNIRT), spatial smoothing (8 mm FWHM), and grand mean intensity normalisation. Six rigid-body motion parameters were included as nuisance regressors. The full preprocessing pipeline is provided in Supplementary information A.7.

4.2.5 First-level statistical modelling

First-level GLMs were estimated using FSL FEAT (v6.0.7.13). The preprocessed and spatially normalised BOLD time series were used as input. Time series were pre-whitened using FILM (FMRIB's improved linear model) to account for temporal autocorrelation. High-pass temporal filtering (200 s cutoff) was applied within FEAT to both the BOLD time series and the design matrix, ensuring consistent filtering of data and model.

Onset times of PC R-peaks were modelled as stick functions and convolved with the canonical double-gamma hemodynamic response function (HRF). Nuisance regressors comprised the six rigid-body motion parameters derived from MCFLIRT (three translations, three rotations). Two contrasts were specified for each participant: PCs $>$ reference (BOLD signal increases) and PCs $<$ reference (BOLD signal decreases).

For the reference condition we modelled regular sinus beat onsets as an explicit stick-function regressor convolved with the canonical HRF. This contrast directly compares hemodynamic responses associated with PCs to those associated with regular cardiac events ("sinus rhythm"), effectively isolating PC-specific neural activity from the continuous heartbeat-related BOLD signal and providing the most conceptually informative measure of PC-specific brain responses.

4.2.6 Group-level statistical inference

Given the small sample size ($N = 11$), non-parametric permutation testing was used as the primary inferential framework, implemented in FSL randomise [54]. At $N = 11$, exhaustive sign-flipping yields exactly $2^{11} = 2048$ unique permutations, constituting an exact permutation test that requires no distributional assumptions. TFCE was applied to combine voxel-level statistics with information about local spatial extent, without reliance on an arbitrary cluster-forming threshold. Statistical maps were thresholded at an FWE-corrected $p < 0.05$.

Corroborative parametric analyses were conducted using FLAME 1+2 [55, 56], which employs MCMC (Markov Chain Monte Carlo) sampling for accurate estimation of between-subject variance, and FLAME 1 [55], an ordinary least-squares mixed-effects approach serving as the most conservative parametric check; both with $Z > 3.1$ and GRF (Gaussian Random Field)-corrected cluster $p < 0.05$ (Supplementary Fig. 5 and Tables 4–5). To validate parametric inference, normality of first-level contrast estimates was confirmed. Details and results are reported in Supplementary information A.8 and Supplementary Fig. 13.

Effect sizes were estimated for significant main clusters of the primary analysis (randomise, $N = 11$, PCs < regular heartbeats) and were assessed using Harvard-Oxford probabilistic atlas masks ($\geq 25\,\%$ probability threshold) rather than single-voxel peaks, avoiding dependence on an arbitrarily chosen extraction radius.

4.2.7 PC subtype specificity analysis

Based on each participant's 24-hour Holter ECG, participants were classified post hoc according to their dominant PC morphology into three subgroups: PVC-dominant ($> 95\,\%$ PVCs; $N = 7$), PAC-dominant ($< 10\,\%$ PVCs; $N = 3$), and mixed ($N = 1$). This stratification reflects the observation that patients with frequent PCs typically display a predominant morphological subtype that remains consistent across recording sessions, as evidenced by the strongly skewed distributions in our sample (10 of 11 participants showed $> 95\,\%$ or $< 10\,\%$ PVCs).

To assess subtype specificity in fMRI BOLD response, exploratory FLAME 1+2 analyses were conducted separately for PVC-dominant ($N = 7$) and PAC-dominant ($N = 3$) subgroups (one participant with mixed PVC/PAC contributions excluded; Supplementary Fig. 6 and Supplementary Table 6). Given the very small PAC-dominant subgroup, those results are substantially underpowered and reported descriptively only.

4.2.8 Atlas labelling

Significant clusters were anatomically labelled using the Harvard-Oxford Cortical and Subcortical Structural Atlases as distributed with FSL (v6.0.7.13; [57]), via a custom Python script using nibabel. For each cluster, the anatomical label was queried at both the peak voxel and the centre of gravity (COG) in MNI152

standard space. Single best-matching region labels were obtained from the 2 mm maximum probability atlas thresholded at 25 %, and probabilistic overlap percentages from the 1 mm probabilistic atlas, consistent with FSLeyes default behaviour (Supplementary information A.7 for full atlas file specifications). Only regions contributing ≥ 5 % of probabilistic atlas overlap at the respective coordinate are reported; regions below this threshold are listed as unlabelled. We report for each cluster: peak MNI coordinates, the primary test statistic (TFCE score for randomise/TFCE analyses; Z-statistic for FLAME 1+2 and FLAME 1 analyses), cluster volume in voxels, and the probabilistic anatomical label with associated percentage at peak and COG.

Data availability

Anonymised data can be requested by application to the LIFE-Study Department (https://ldp.life.uni-leipzig.de/).

Code availability

The underlying source code for the EEG and fMRI analyses of the paper can be found on GitHub (https://github.com/PiaRe/NeuralSignaturesPrematureHeartbeats-EEG, https://github.com/evagreschke/NeuralSignaturesPrematureHeartbeats-fMRI).

References

[1] Critchley, H. D., Wiens, S., Rotshtein, P., Öhman, A. & Dolan, R. J. Neural systems supporting interoceptive awareness. *Nat. Neurosci.* **7**, 189–195 (2004).

[2] Seth, A. K., Suzuki, K. & Critchley, H. D. An Interoceptive Predictive Coding Model of Conscious Presence. *Front. Psychol.* **2** (2012).

[3] Yoshimoto, A., Morikawa, S., Kato, E., Takeuchi, H. & Ikegaya, Y. Top-down brain circuits for operant bradycardia. *Science* **384**, 1361–1368 (2024).

[4] von Rotz, M. *et al.* Risk factors for premature ventricular contractions in young and healthy adults. *Heart* **103**, 702–707 (2017).

[5] Conen, D. *et al.* Premature Atrial Contractions in the General Population: Frequency and Risk Factors. *Circulation* **126**, 2302–2308 (2012).

[6] Loeffler, M. *et al.* The LIFE-Adult-Study: Objectives and design of a population-based cohort study with 10,000 deeply phenotyped adults in Germany. *BMC Public Health* **15**, 691 (2015).

[7] Schandry, R., Sparrer, B. & Weitkunat, R. From the heart to the brain: A study of heartbeat contingent scalp potentials. *Int. J. Neurosci.* **30**, 261–275 (1986).

[8] Park, H.-D., Correia, S., Ducorps, A. & Tallon-Baudry, C. Spontaneous fluctuations in neural responses to heartbeats predict visual detection. *Nat. Neurosci.* **17**, 612–618 (2014).

[9] Montoya, P., Schandry, R. & Müller, A. Heartbeat evoked potentials (HEP): Topography and influence of cardiac awareness and focus of attention. *Electroencephalogr. Clin. Neurophysiol. Potentials Sect.* **88**, 163–172 (1993).

[10] Allen, P. J., Polizzi, G., Krakow, K., Fish, D. R. & Lemieux, L. Identification of EEG Events in the MR Scanner: The Problem of Pulse Artifact and a Method for Its Subtraction. *NeuroImage* **8**, 229–239 (1998).

[11] Steinfath, P. *et al.* Validating genuine changes in heartbeat-evoked potentials using pseudotrials and surrogate procedures. *Imaging Neurosci.* **3** (2025).

[12] Vecchietti, S., Langley, P., Severi, S., Cavalcanti, S. & Murray, A. Effect of premature ventricular beats on manual and automatic repolarization measurements. *J. Electrocardiol.* **37**, 181–189 (2004).

[13] Reiffel, A. J. & Reiffel, J. A. QT Prolongation Following Ectopic Beats: Initial Data Regarding the Upper Limit of Normal with Possible Implications for Antiarrhythmic Therapy and Concealed (Unexpressed) Long QT. *J. Atr. Fibrillation* **1**, 520 (2009).

[14] Craig, A. D. How do you feel? Interoception: The sense of the physiological condition of the body. *Nat. Rev. Neurosci.* **3**, 655–666 (2002).

[15] Garfinkel, S. N. *et al.* Interoceptive dimensions across cardiac and respiratory axes. *Philos. Trans. R. Soc. B Biol. Sci.* **371**, 20160014 (2016).

[16] Brener, M. I., Burkhoff, D., Basir, M. B. & Alqarqaz, M. Pressure-Volume Analysis Illustrating the Mechanisms of Short-Term Hemodynamic Effects Produced by Premature Ventricular Contractions. *Circ. Heart Fail.* **14**, e007766 (2021).

[17] Billet, S. *et al.* Hemodynamic consequences of premature ventricular contractions: Association of mechanical bradycardia and postextrasystolic potentiation with premature ventricular contraction-induced cardiomyopathy. *Heart Rhythm* **16**, 853–860 (2019).

[18] Voss, A. *et al.* Postextrasystolic regulation patterns of blood pressure and heart rate in patients with idiopathic dilated cardiomyopathy. *J. Physiol.* **538**, 271–278 (2002).

[19] Critchley, H. D. *et al.* Human cingulate cortex and autonomic control: Converging neuroimaging and clinical evidence. *Brain* **126**, 2139–2152 (2003).

[20] Vogt, B. A. Pain and emotion interactions in subregions of the cingulate gyrus. *Nat. Rev. Neurosci.* **6**, 533–544 (2005).

[21] Park, H.-D. & Blanke, O. Heartbeat-evoked cortical responses: Underlying mechanisms, functional roles, and methodological considerations. *NeuroImage* **197**, 502–511 (2019).

[22] Cooper, M. W. Postextrasystolic potentiation. Do we really know what it means and how to use it? *Circulation* **88**, 2962–2971 (1993).

[23] Kern, M., Aertsen, A., Schulze-Bonhage, A. & Ball, T. Heart cycle-related effects on event-related potentials, spectral power changes, and connectivity patterns in the human ECoG. *NeuroImage* **81**, 178–190 (2013).

[24] Li, D. *et al.* Asphyxia-activated corticocardiac signaling accelerates onset of cardiac arrest. *Proc. Natl. Acad. Sci.* **112** (2015).

[25] García-Cordero, I. *et al.* Attention, in and Out: Scalp-Level and Intracranial EEG Correlates of Interoception and Exteroception. *Front. Neurosci.* **11**, 411 (2017).

[26] Ainley, V., Apps, M. A. J., Fotopoulou, A. & Tsakiris, M. 'Bodily precision': A predictive coding account of individual differences in interoceptive accuracy. *Philos. Trans. R. Soc. B Biol. Sci.* **371**, 20160003 (2016).

[27] Swenne, C. A. & Shusterman, V. Neurocardiology: Major mechanisms and effects. *J. Electrocardiol.* **88**, 153836 (2025).

[28] Marcus, G. M. Evaluation and Management of Premature Ventricular Complexes. *Circulation* **141**, 1404–1418 (2020).

[29] Pfeiffer, C. & De Lucia, M. Cardio-audio synchronization drives neural surprise response. *Sci. Rep.* **7**, 14842 (2017).

[30] Banellis, L. & Cruse, D. Skipping a Beat: Heartbeat-Evoked Potentials Reflect Predictions during Interoceptive-Exteroceptive Integration. *Cereb. Cortex Commun.* **1**, tgaa060 (2020).

[31] Medford, N. & Critchley, H. D. Conjoint activity of anterior insular and anterior cingulate cortex: Awareness and response. *Brain Struct. Funct.* **214**, 535–549 (2010).

[32] Fitzgerald, K. & Todd, J. Making Sense of Mismatch Negativity. *Front. Psychiatry* **11**, 468 (2020).

[33] Kumral, D. *et al.* Attenuation of the Heartbeat-Evoked Potential in Patients With Atrial Fibrillation. *JACC Clin. Electrophysiol.* **8**, 1219–1230 (2022).

[34] Salvato, G., Richter, F., Sedeño, L., Bottini, G. & Paulesu, E. Building the bodily self-awareness: Evidence for the convergence between interoceptive and exteroceptive information in a multilevel kernel density analysis study. *Hum. Brain Mapp.* **41**, 401–418 (2020).

[35] Lovelace, J. W. *et al.* Vagal sensory neurons mediate the Bezold–Jarisch reflex and induce syncope. *Nature* **623**, 387–396 (2023).

[36] Steinfath, P. *et al.* Heartbeat-Evoked Responses in M/EEG: A Systematic Review of Methods With Suggestions for Analysis and Reporting. *Psychophysiology* **63**, e70297 (2026).

[37] Gray, M. A. *et al.* A cortical potential reflecting cardiac function. *Proc. Natl. Acad. Sci.* **104**, 6818–6823 (2007).

[38] Coll, M.-P., Hobson, H. & Murphy, J. Systematic review and meta-analysis of the relationship between the heartbeat-evoked potential and interoception. Preprint at https://doi.org/10.31234/osf.io/g2zhc (2020).

[39] Posse, S. *et al.* Enhancement of BOLD-contrast sensitivity by single-shot multi-echo functional MR imaging. *Magn. Reson. Med.* **42**, 87–97 (1999).

[40] Feinberg, D. A. *et al.* Multiplexed Echo Planar Imaging for Sub-Second Whole Brain FMRI and Fast Diffusion Imaging. *PLoS ONE* **5**, e15710 (2010).

[41] Vaglio, M. *et al.* CER-S, an ECG Platform for the Management of Continuous ECG Recordings and Databases. *Comput. Cardiol. Conf. CinC* (2022).

[42] Delorme, A. & Makeig, S. EEGLAB: An open source toolbox for analysis of single-trial EEG dynamics including independent component analysis. *J. Neurosci. Methods* **134**, 9–21 (2004).

[43] Oostenveld, R., Fries, P., Maris, E. & Schoffelen, J.-M. FieldTrip: Open Source Software for Advanced Analysis of MEG, EEG, and Invasive Electrophysiological Data. *Comput. Intell. Neurosci.* **2011**, 1–9 (2011).

[44] Buot, A., Azzalini, D., Chaumon, M. & Tallon-Baudry, C. Does stroke volume influence heartbeat evoked responses? *Biol. Psychol.* **165**, 108165 (2021).

[45] Chaumon, M., Bishop, D. V. & Busch, N. A. A practical guide to the selection of independent components of the electroencephalogram for artifact correction. *J. Neurosci. Methods* **250**, 47–63 (2015).

[46] Maris, E. & Oostenveld, R. Nonparametric statistical testing of EEG- and MEG-data. *J. Neurosci. Methods* **164**, 177–190 (2007).

[47] Huang, Y., Parra, L. C. & Haufe, S. The New York Head—A precise standardized volume conductor model for EEG source localization and tES targeting. *NeuroImage* **140**, 150–162 (2016).

[48] Fonov, VS., Evans, AC., McKinstry, RC., Almli, CR. & Collins, DL. Unbiased nonlinear average age-appropriate brain templates from birth to adulthood. *NeuroImage* **47**, S102 (2009).

[49] Pascual-Marqui, R. D. Discrete, 3D distributed, linear imaging methods of electric neuronal activity. Part 1: Exact, zero error localization. Preprint at https://arxiv.org/abs/0710.3341 (2007).

[50] Haufe, S. & Ewald, A. A Simulation Framework for Benchmarking EEG-Based Brain Connectivity Estimation Methodologies. *Brain Topogr.* **32**, 625–642 (2019).

[51] Kapralov, N. *et al.* Sensorimotor brain–computer interface performance depends on signal-to-noise ratio but not connectivity of the mu rhythm in a multiverse analysis of longitudinal data. *J. Neural Eng.* **21**, 056027 (2024).

[52] Gorgolewski, K. J. *et al.* The brain imaging data structure, a format for organizing and describing outputs of neuroimaging experiments. *Sci. Data* **3**, 160044 (2016).

[53] Li, X., Morgan, P. S., Ashburner, J., Smith, J. & Rorden, C. The first step for neuroimaging data analysis: DICOM to NIfTI conversion. *J. Neurosci. Methods* **264**, 47–56 (2016).

[54] Winkler, A. M., Ridgway, G. R., Webster, M. A., Smith, S. M. & Nichols, T. E. Permutation inference for the general linear model. *NeuroImage* **92**, 381–397 (2014).

[55] Beckmann, C. F., Jenkinson, M. & Smith, S. M. General multilevel linear modeling for group analysis in FMRI. *NeuroImage* **20**, 1052–1063 (2003).

[56] Woolrich, M. W., Behrens, T. E., Beckmann, C. F., Jenkinson, M. & Smith, S. M. Multilevel linear modelling for FMRI group analysis using Bayesian inference. *NeuroImage* **21**, 1732–1747 (2004).

[57] Jenkinson, M., Beckmann, C. F., Behrens, T. E., Woolrich, M. W. & Smith, S. M. FSL. *NeuroImage* **62**, 782–790 (2012).

[58] Andersson, J. L., Skare, S. & Ashburner, J. How to correct susceptibility distortions in spin-echo echo-planar images: Application to diffusion tensor imaging. *NeuroImage* **20**, 870–888 (2003).

[59] Jenkinson, M., Bannister, P., Brady, M. & Smith, S. Improved optimization for the robust and accurate linear registration and motion correction of brain images. *NeuroImage* **17**, 825–841 (2002).

[60] Greve, D. N. & Fischl, B. Accurate and robust brain image alignment using boundary-based registration. *NeuroImage* **48**, 63–72 (2009).

Acknowledgements

This study was supported by the LIFE-Leipzig Research Center for Civilization Diseases, Leipzig University. LIFE is funded by the European Union, the European Regional Development Fund (ERDF), the European Social Fund (ESF), and the Free State of Saxony within the framework of the excellence initiative. We thank all study participants and the LIFE team for making this study possible. We thank the Max Planck Research Group Pain Perception, MPI CBS for providing the MRI-artefact cleaning script for within- scanner ECG recordings, and the Center for Magnetic Resonance Research (CMRR, University of Minnesota) for the readCMRRPhysio script used to extract within-scanner PPG data. We also acknowledge dcm2niix (Rorden Lab) for DICOM-to-BIDS conversion.

Author contributions

A.V. conceptualised research goals. P.R., T.P.S. and P.-H.K. selected and preprocessed the EEG data. P.R. analysed the EEG data and wrote the manuscript. E.G., T.U., H.S.F. and U.L. recruited the fMRI participants. E.G. recorded, preprocessed and analysed the fMRI data and wrote the fMRI part of the manuscript. All authors reviewed and edited the manuscript and further read and agreed to the submitted version of the manuscript.

Competing interests

The authors declare no competing interests.

Appendix A Supplementary information

A.1 Morphology of the PVC

Since PVCs are associated with variations in the morphology of the QRS complex and the polarity of the T-wave (both positive and negative), we took special care to account for potential CFAs in the EEG. In theory, averaging over trials with mixed CFA polarity could lead to CFA cancellation and thus to a flattened HEP. Therefore, the analysis was repeated on two subsets of participants categorised by the polarity of the T-wave in their ECG signals. Analysis of both subsets confirmed the initial finding, showing a significant difference between conditions ($p < 0.05$) and similar clusters (Supplementary Fig. 1). This indicates that CFAs do not account for the diminished HEP amplitude.

A.2 ECG analysis

The ECGs in PVC and PC+1 were analysed to assess whether potential differences in CFAs might have affected the differences in HEPs reported above. A significant difference in ECG between PVC and PVC-3 was most pronounced in the time window before the R-peak from −120 ms to −100 ms (Monte Carlo $p < 0.0144$), from −90 ms to −10 ms (Monte Carlo $p < 0.0096$), and after the T-wave in the time window from 410 ms to 560 ms (Monte Carlo $p < 0.0012$, Supplementary Fig. 14).

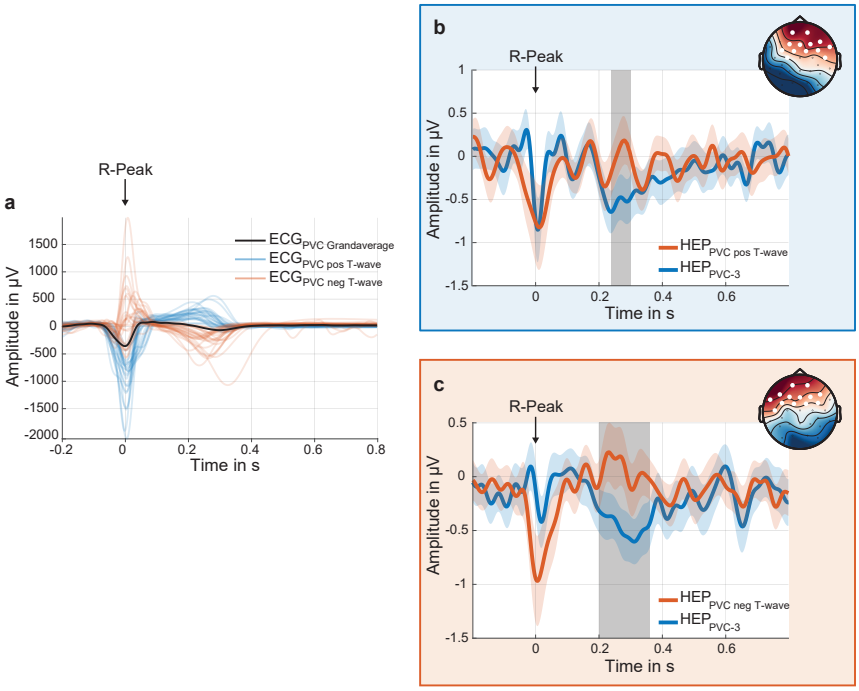
The comparison of the ECG signal between the PC+1 condition and the reference (PC-3) revealed a significant difference, most pronounced in the time window from −200 ms to 600 ms (Monte Carlo $p < 0.023$, Supplementary Fig. 15). Notably, the T-wave was delayed and reduced in amplitude (QT-prolongation [12, 13]), while EEG analyses showed an earlier and larger peak. This temporal mismatch makes it unlikely that later CFAs in the T-wave could account for the earlier EEG differences, arguing against ECG differences as the sole source of the observed HEP effects (Supplementary Fig. 15).

A.3 Controlling for CFA with correlation analyses

To assess the effect of possible residual heartbeats and CFAs on the differences between the two conditions, we performed correlation analyses between the ECG and EEG, similar to those by Buot et al. [44]. This step was crucial to ensure that the variations detected in EEG signals were not merely reflections of cardiac artefacts but genuine neural activity differences.

A.3.1 Cluster-based permutation analysis of entire time window

For all time courses and each participant, the epoch-wise difference (Δ) between the conditions was calculated. The empirical Spearman correlation between each averaged Δ EEG channel and the averaged Δ ECG channel for each time point of the entire time window and each participant was then determined and Fisher-transformed. To estimate the correlation at the chance level, the associations



Supplementary Fig. 1: T-wave polarity does not account for the reduced heartbeat-evoked potential in PVC. Control analysis for CFA of polymorph PVC. **(a)** Polymorph appearance of PVC. Blue lines represent participantwise averages of PVC with positive "T-waves" and orange lines with negative "T-waves" respectively. The black line shows the grand average over all participants. **(b)** Significant difference between HEPs of subgroup PVC with positive "T-waves" and reference condition ($p < 0.05$) averaged over the cluster of white marked electrodes. **(c)** Significant difference between HEPs of subgroup PVC with negative "T-waves" and reference condition ($p < 0.05$) averaged over the cluster of white marked electrodes. The grey-shaded area highlights the time window of the found cluster. The colour-shaded regions around the lines mark the ±1 SEM.

between time points were permuted (e.g., time point i in the time course of electrode Fp1 was reallocated to time point j in the ECG-time course) and the correlation coefficient was recalculated. After performing this permutation and recalculation 100 times, the median of the correlation coefficients was taken and statistically compared with the empirical correlation using a cluster-based permutation test at the group level.

A.3.2 Analysis of averaged time window

In addition, a second correlation analysis focused on the time window in which the primary difference between conditions was identified in the EEG. This time window of the EEG and ECG signals was selected and averaged over time and then over epochs. The empirical Pearson correlation coefficients across participants and electrodes between the ECG and all EEG channels were calculated and FDR-corrected.

ECG differences did not significantly correlate with EEG differences over the entire PVC time window (Supplementary Fig. 16).

Analysing the time window in which main differences between conditions were found (220 ms to 350 ms), the EEG difference at electrode FT9 correlated significantly ($\rho = -0.49$; $p_{\mathrm{FDR}} < 0.05$) with the ECG difference of the PVC conditions (Supplementary Fig. 17). No significant correlation was found for any of the other electrodes.

This suggests that the EEG effects observed in the PVC condition are not primarily due to variations in the ECG.

Performing the same analyses on the PC+1 condition, no significant correlation was found either for the analysis of the entire time window or for the selected averaged time window from 130 ms to 200 ms ($p_{\mathrm{FDR}} > 0.05$, Supplementary Figs. 18 and 19).

This also implies that the EEG changes observed during the PC+1 condition are not primarily attributable to differences in the ECG.

A.4 Control analyses for T-wave amplitude

We conducted a control analysis to ensure that the observed differences in PC+1 in the EEG were not due to variations in the ECG. These analyses involved matching epochs based on the T-peak amplitude. We only applied the matching for the PC+1 condition, as the impact of the T-wave projection on the HEP in the PC condition was already tested in Section A.1.

We extracted the maximum absolute value for PC+1 within the 200 ms to 400 ms time window and matched it with the corresponding N and PC-3 beat values.

We solved the linear assignment problem with a predefined cost for unmatched epochs. Epochs within PC+1 that lacked a counterpart were left unmatched and excluded from further analysis. The cost was iteratively adapted and adjusted until there was no significant difference in the dependent t-test between the PC+1 T-peak amplitude values and the matched N/PC-3 values (Supplementary Table 9). After that, the cluster-based permutation t-tests for the EEG data were repeated.

The two conditions remained significantly different. We found one positive ($p < 0.0004$; CP5, CP6, TP9, TP10, P3, P4, P7, P8, O1, O2, PO9, PO10) and one negative cluster ($p < 0.002$; Fp1, Fp2, F3, F4, F7, F8, Fz, FC1, FC2, FC5, FC6, C4, Cz) approximately between 130 ms to 290 ms (Supplementary Fig. 20).

This shows that the EEG data still has a significant difference independent of the T-wave amplitude.

A.5 Comparison to matched control group

Further, we conducted a control-group analysis to investigate a potential difference in the HEP based on regular heartbeats between participants with premature contractions and those without. Therefore, we matched the premature contraction participants ($N = 103$) with control participants ($N = 103$) who met the inclusion and exclusion criteria (Supplementary List 1). We used the k-nearest-neighbour algorithm for matching based on body mass index (BMI), age, diastolic and systolic blood pressure, where available, and exact matching for sex (Supplementary Fig. 21).

The control-group analysis revealed no significant difference in sinus beats between the PAC and control groups ($p > 0.3$). However, the PVC group showed a significant difference, with a negative cluster, in the time window of 340 ms to 450 ms over the F7, FC5, and T7 electrodes ($p < 0.03$, Supplementary Fig. 22). The ECG also showed a significant difference, with the early most pronounced difference ranging from 110 ms to 280 ms (Monte Carlo $p < 0.0004$, Supplementary Fig. 23). Therefore, although the ECG also showed a significant effect, the main difference occurred in a different time window than the EEG effect. Furthermore, although the ECG of the PVC group shows a lower T-wave, the HEP exhibits a higher amplitude, suggesting that the differences in HEPs between conditions are unlikely to be artefactual.

A.6 Additional MRI sequences

In addition to the sequences used in our analysis, participants underwent several additional MRI acquisitions. A T1-weighted MPRAGE sequence (1 mm isotropic, TR = 2300 ms, TE = 2.98 ms, TI = 900 ms, flip angle = 9°) was acquired for anatomical reference. A field map sequence was acquired for B_0 distortion correction using TOPUP (FSL). These sequences were used during preprocessing, as described in the Methods section. Additional sequences (fMRI task data, 3D T2-weighted SPACE, and diffusion-weighted imaging) were acquired but were not utilised in the present analysis (Supplementary information A.7).

A.7 FSL software and preprocessing pipeline

All fMRI analyses were performed using FSL 6.0.7.13 (FMRIB Software Library [57]). Key tools included: TOPUP for susceptibility-induced distortion correction; FLIRT for linear registration; FNIRT for nonlinear registration to MNI152 standard space; FEAT for first-level GLM modelling; FLAME 1+2 and FLAME 1 for group-level mixed-effects inference; and randomise with TFCE for non-parametric permutation testing. Harvard-Oxford Cortical and Subcortical Structural Atlases (2 mm maximum probability atlas, 25 % threshold) were

used for anatomical labelling. For probabilistic overlap queries in FSLeyes, the 1 mm probabilistic atlas with raw (non-normalised) probability values was used. Full atlas file specifications are available at https://fsl.fmrib.ox.ac.uk/fsl/fslwiki/Atlases.

Preprocessing pipeline. The following steps were applied sequentially.

Distortion correction. A B_0 field map was estimated from the pair of opposing-phase-encoding EPI acquisitions (AP and PA) using TOPUP [58] and applied to correct susceptibility-induced geometric distortions in the functional data before all subsequent steps.

Anatomical preprocessing. Brain extraction of the T1-weighted anatomical image was performed using BET (Brain Extraction Tool). The skull-stripped anatomical image served as the registration target for functional-structural alignment and as the intermediate space for normalisation to MNI152 standard space (2 mm isotropic). Normalisation proceeded in two steps: first, a linear affine registration (12 degrees of freedom) was performed using FLIRT [59]; this was then used to initialise nonlinear registration using FNIRT (warp resolution: 10 mm). Visual inspection of all warp fields and normalised images confirmed successful spatial normalisation for all participants, including alignment of ventricular boundaries and cortical surfaces to the MNI152 template.

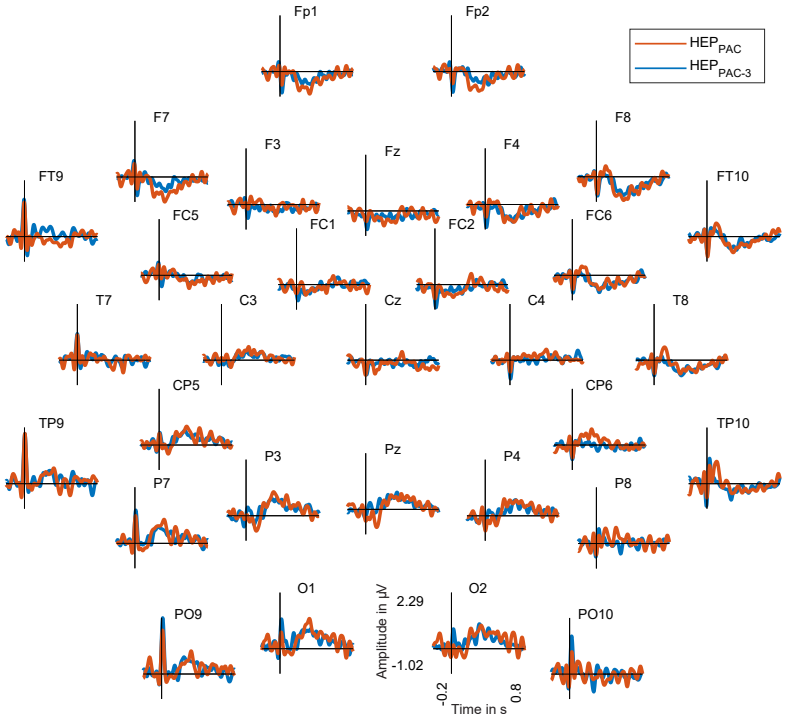
Functional preprocessing. For each participant's resting-state scan, a BOLD reference volume was generated and used as the target for head-motion correction with MCFLIRT [59]. Slice-timing correction was applied using a custom slice-timing file specifying the acquisition time of each slice relative to the start of the volume repetition time, rather than assuming a standard ascending or interleaved acquisition order. Functional data were co-registered to the participant's T1-weighted image using boundary-based registration (BBR) [60]. Functional images were transformed to MNI152 standard space (2 mm isotropic) by concatenating the functional-to-structural (BBR) and structural-to-MNI (FNIRT) transformations and applying them sequentially. Finally, the functional data underwent spatial smoothing (8 mm FWHM isotropic Gaussian kernel) and grand mean intensity normalisation.

First-level nuisance regressors. Six rigid-body motion parameters derived from MCFLIRT (three translations, three rotations) were included as nuisance regressors in each participant's first-level general linear model (GLM). No additional physiological or data-driven noise regressors were applied. Motion parameter traces were inspected visually for all participants; no participant was excluded on grounds of excessive head motion.

A.8 Normality assessment at primary regions of interest

Normality of first-level contrast estimates (PCs < regular heartbeats) was assessed within three results-independent Harvard-Oxford probabilistic atlas masks ($\geq 25\,\%$ probability threshold) across participants ($N = 11$) using the Shapiro-Wilk test. No violation of normality was observed at any of the three primary ROIs (right insular cortex: $W = 0.952$, $p = 0.673$; left insular cortex: $W = 0.895$, $p = 0.162$; ACC: $W = 0.978$, $p = 0.952$; Supplementary Fig. 13),

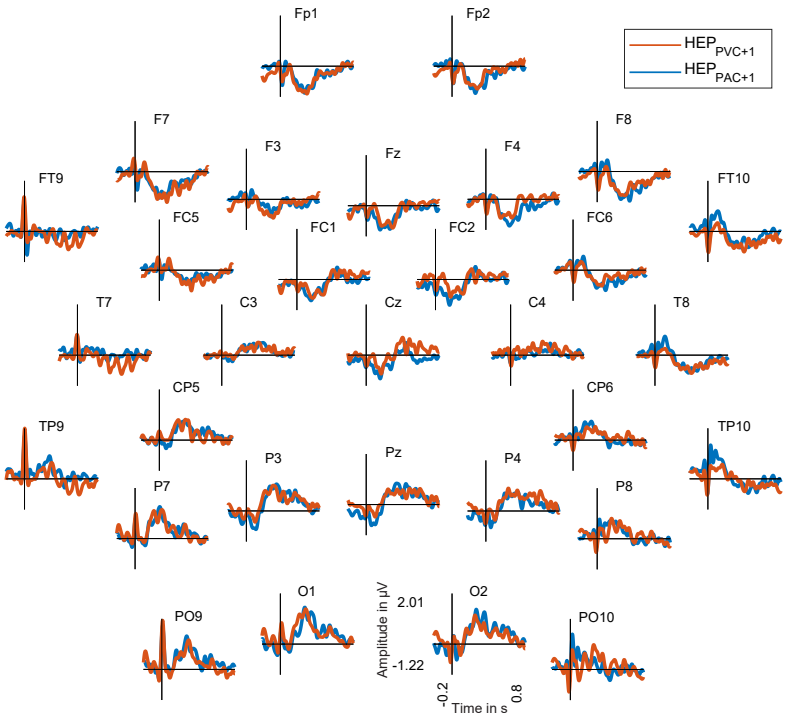
supporting the validity of parametric inference in these regions. Note that the primary inference is based on non-parametric permutation testing (randomise/TFCE), which requires no distributional assumptions given the small sample size ($N = 11$; see Section 4.2.6); the normality assessment reported here applies specifically to the corroborative FLAME analyses.



Supplementary Fig. 2: No significant heartbeat-evoked potential difference between PAC and the reference condition. No significant differences ($p > 0.2$) in HEP in the time domain between condition PAC and PAC-3.

Supplementary Table 1: Heartbeat-evoked potential differences are robust across preprocessing pipelines. Cluster Statistics over the multiverse preprocessing analyses of HEP in the time domain.

	Baseline	ICA	Significant	Latency	Cluster Electrodes	Polarity	Sum(t)	Monte Carlo p
PVC	−150 ms to −50 ms before reference condition	yes	yes	224 ms to 332 ms	C3,CP5,CP6,TP9,TP10,P3,P4,P7,P8,O1,O2,PO9,PO10	negative	-916	0.0008
				226 ms to 348 ms	Fp1,Fp2,F3,F4,F7,F8,Fz,FC1,FC5,FC6,C3,T7,FT9	positive	1348	0.0002
PAC			no	92 ms to 120 ms	F8,FC6,T8,FT10,CP6,TP10,P8	negative	-224	0.2258
				134 ms to 334 ms	P7,O1,PO9	positive	45	0.9536
PC			yes	258 ms to 310 ms	C4,CP5,CP6,TP10,P3,P4,P7,P8,O1,O2,PO9,PO10	negative	-408	0.0362
				256 ms to 334 ms	Fp1,Fp2,F3,F4,F7,F8,Fz,FC1,FC5,T7,FT9	positive	822	0.0006
PVC+1			yes	138 ms to 204 ms	Fp1,Fp2,F3,F4,F8,Fz,FC1,FC2,FC6,C4,T8,Cz	negative	-1115	0.0004
				146 ms to 214 ms	T7,CP5,TP9,P3,P7,P8,O1,O2,PO9,PO10	positive	806	0.0004
PAC+1			yes	126 ms to 178 ms	Fp1,Fp2,F3,F4,F7,F8,Fz,FC1,FC2,FC5,FC6,Cz	negative	-760	0.0002
				128 ms to 180 ms	T8,FT10,CP5,CP6,TP9,TP10,P4,P7,P8,O1,O2,PO9,PO10	positive	464	0.0013
PC+1			yes	128 ms to 208 ms	Fp1,Fp2,F3,F4,F7,F8,Fz,FC1,FC2,FC6,C4,Cz	negative	-1454	0.0002
				132 ms to 186 ms	CP5,CP6,TP9,TP10,P3,P4,P7,P8,O1,O2,PO9,PO10	positive	800	0.0002
PVC	−150 ms to −50 ms before condition of interest	yes	yes	224 ms to 280 ms	C3, CP5, TP9, P3, P7, O1, PO9	negative	-417	0.0053
				236 ms to 308 ms	Fp1, Fp2, F3, F4, F7, F8, Fz, FC1, FC5, FC6, T7	positive	549	0.0194
PAC			no	302 ms to 338 ms	T7,CP5,TP9,P7,O1,PO9	negative	-173	0.3879
				296 ms to 306 ms	Fp2,F4,F8,FC6,FT10	positive	60	0.8352
PC			yes	234 ms to 420 ms	C3,C4,Cz,CP5,CP6,TP9,TP10,P3,P4,P7,P8,O1,O2,PO9,PO10	negative	-1896	0.0006
				−52 ms to −16 ms	F4,F8,FC2,FC6,C4,T8,FT10,CP6,TP10,P8	negative	-548	0.0218
				208 ms to 310 ms	Fp1,Fp2,F3,F4,F7,F8,Fz,FC1,FC2,FC5	positive	915	0.0030
PVC+1			yes	136 ms to 196 ms	Fp1, Fp2, F3, F4, F8, Fz, FC1, FC2, FC6, C4, Cz	negative	-831	0.0006
				144 ms to 212 ms	CP5, TP9, P3, P4, P7, P8, Pz, O1, O2, PO9, PO10	positive	720	0.0016
PAC+1			yes	126 ms to 174 ms	Fp1, Fp2, F3, F4, F7, F8, Fz, FC1, FC2, FC5, FC6, Cz	negative	-641	0.0024
				126 ms to 172 ms	CP5, TP9, P4, P7, P8, Pz, O1, O2, PO9, PO10	positive	418	0.0244
PC+1			yes	130 ms to 196 ms	Fp1, Fp2, F3, F4, F7, F8, Fz, FC1, FC2, FC5, FC6, C4, Cz	negative	-1175	0.0002
				−200 ms to −156 ms	Fp1, Fp2, F3, F4, F7, Fz, FC1, FC2, FC5, C3, Cz	negative	-449	0.0236
				128 ms to 278 ms	T7, CP5, TP9, TP10, P3, P4, P7, P8, Pz, O1, O2, PO9, PO10	positive	1509	0.0002
PVC	no baseline correction	yes	yes	224 ms to 332 ms	C3, CP5, CP6, TP9, TP10, P3, P4, P7, P8, O1, O2, PO9, PO10	negative	-916	0.0014
				226 ms to 348 ms	Fp1, Fp2, F3, F4, F7, F8, Fz, FC1,FC5, FC6, C3, T7, FT9	positive	1348	0.0002
PAC			no	92 ms to 120 ms	F8,FC6,T8,FT10,CP6,TP10,P8	negative	-224	0.2258
				134 ms to 144 ms	P7,O1,PO9	positive	45	0.9514
PC			yes	258 ms to 310 ms	C4,CP5,CP6,TP10,P3,P4,P7,P8,O1,O2,PO9,PO10	negative	-408	0.0362
				256 ms to 334 ms	Fp1,Fp2,F3,F4,F7,F8,Fz,FC1,FC5,T7,FT9	positive	822	0.0006
PVC+1			yes	138 ms to 204 ms	Fp1, Fp2, F3, F4, F8, Fz, FC1, FC2, FC6, C4, T8, Cz	negative	-1115	0.0002
				146 ms to 214 ms	T7, CP5, TP9, P3, P7, P8, O1, O2, PO9, PO10	positive	806	0.0002
PAC+1			yes	128 ms to 176 ms	Fp1, Fp2, F3, F4, F7, F8, Fz, FC1, FC2, FC5, FC6, Cz	negative	-683	0.0006
				134 ms to 174 ms	CP5, CP6, TP9, TP10, P7, P8, O1, O2, PO9, PO10	positive	382	0.0230
PC+1			yes	130 ms to 204 ms	Fp1, Fp2, F3, F4, F7, F8, Fz, FC1, FC2, FC6, C4, Cz	negative	-1344	0.0002
				244 ms to 280 ms	Fp1, Fp2, F3, F4, F7, F8, Fz, FC1, FC2, FC5, FC6, Cz	negative	-447	0.0134
				132 ms to 184 ms	CP5, CP6, TP9, TP10, P3, P4, P7, P8, O1, O2, PO9, PO10	positive	766	0.0008
PVC	−150 ms to −50 ms before reference condition	no	yes	228 ms to 374 ms	C4, CP5, CP6, TP10, P3, P4, P7, P8, Pz, O1, O2, PO9, PO10	negative	-1662	0.0002
				−118 ms to −84 ms	Fp2, F4, F8, FC2, FC6, C4, T8, FT10, CP6, TP10, P8, O2, PO10	negative	-1311	0.0010
				146 ms to 484 ms	Fp1, Fp2, F3, F4, F7, Fz, FC1, FC5, T7, FT9, TP9	positive	2682	0.0002
				−54 ms to −16 ms	F7, FC5, C3, T7, FT9, CP5, TP9, P3, P7, O1, PO9	positive	673	0.0002
PAC			no	302 ms to 338 ms	T7,CP5,TP9,P7,O1,PO9	negative	-173	0.3879
				296 ms to 306 ms	Fp2,F4,F8,FC6,FT10	positive	60	0.8352
PC			yes	234 ms to 420 ms	C3,C4,Cz,CP5,CP6,TP9,TP10,P3,P4,P7,P8,O1,O2,PO9,PO10	negative	-1896	0.0006
				−52 ms to −16 ms	F4,F8,FC2,FC6,C4,T8,FT10,CP6,TP10,P8	negative	-548	0.0218
				208 ms to 310 ms	Fp1,Fp2,F3,F4,F7,F8,Fz,FC1,FC2,FC5	positive	915	0.0030
				136 ms to 214 ms	F4, F8, Fz, FC1, FC2, FC6, C4, Cz	negative	-834	0.0016
PVC+1			yes	−200 ms to −128 ms	F3, FC1, C3, Cz, P3, P4, Pz	negative	-539	0.0128
				−48 ms to 40 ms	F7, FC5, C3, T7, FT9, CP5, TP9, P3, P7, O1, PO9	negative	-533	0.0132
				142 ms to 216 ms	FC1, Cz, P3, P4, Pz, O2	positive	660	0.0056
				−200 ms to −112 ms	FC1, FC2, C3, Cz, P3, P4, P7, Pz, O1, O2, PO9	negative	-887	0.0014
PAC+1			yes	100 ms to 228 ms	F8, FC6, T8, FT10, CP6, TP10, P8, PO10	positive	1017	0.0020
				−4 ms to 82 ms	F8, FC6, T8, FT10, CP6, TP10, P8, PO10	positive	640	0.0092
				14 ms to 298 ms	F4, F8, Fz, FC1, FC2, FC6, C3, C4, Cz, P3, P4, Pz, O2	negative	-2292	0.0002
PC+1			yes	−200 ms to −4 ms	FC1, FC2, C3, C4, Cz, CP5, P3, P4, Pz, O1, O2	negative	-1971	0.0004
				126 ms to 214 ms	T7, CP5, CP6, TP9, TP10, P7, P8, O1, PO9, PO10	positive	910	0.0028



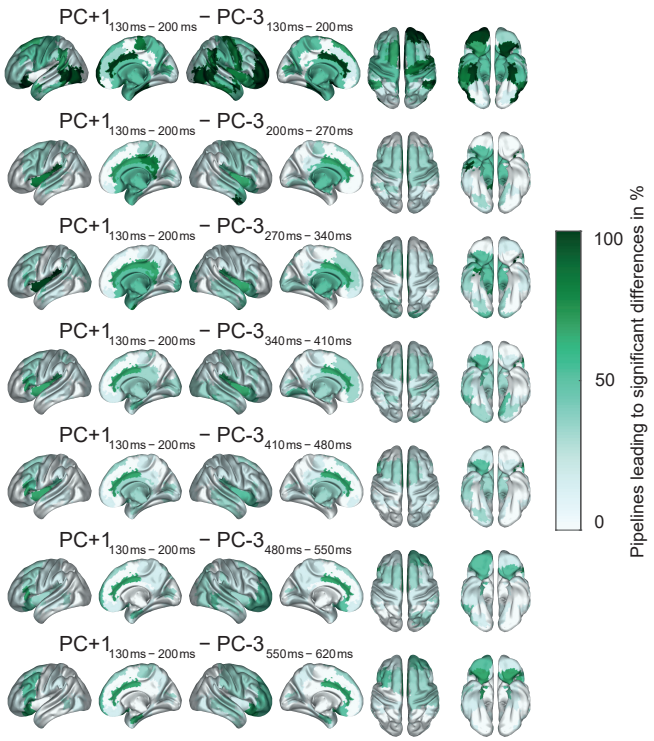
Supplementary Fig. 3: Robust neural effect to the postextrasystolic beat of both premature contraction types. No significant differences ($p > 0.5$) in HEP in the time domain between groups PVC+1 and PAC+1.

Supplementary Table 2: Source-space statistics for the PVC condition across multiverse pipelines. Multiverse source analysis of sources in the PVC condition averaged over the time window with most prominent HEP difference (220 ms to 350 ms). AVG and AVG-SF were compared to aggregate the dipole sources into single ROIs. Cell background shading indicates statistical significance: light grey cells reach the significance threshold ($p < 0.05$, FDR-corrected). The p-value is printed in green when the comparison condition shows greater absolute source activity (|PVC| > |PVC-3|) and in red when it shows smaller absolute source activity (|PVC| < |PVC-3|).

		p-value: paired t-test of |PVC| vs |PVC-3| within each source									
Regularisation Parameter	Aggregation Method	Left Cingulate Gyrus posterior division	Right Cingulate Gyrus posterior division	Left Postcentral Gyrus	Right Postcentral Gyrus	Left Frontal Orbital Cortex	Right Frontal Orbital Cortex	Left Insular Cortex	Right Insular Cortex	Left Cingulate Gyrus anterior division	Right Cingulate Gyrus anterior division
0.5	AVG	0.206	0.156	0.044	0.047	0.083	0.047	0.047	0.206	0.498	0.047
0.5	AVG-SF	0.246	0.171	<0.001	0.003	0.003	0.007	0.019	0.178	0.498	0.028
0.05	AVG	0.958	0.860	0.004	0.098	0.365	0.107	0.018	0.098	0.860	0.098
0.05	AVG-SF	0.943	0.857	0.013	0.047	0.047	0.070	0.013	0.070	0.857	0.070
0.001	AVG	0.918	0.918	0.001	0.098	0.542	0.204	0.007	0.098	0.918	0.418
0.001	AVG-SF	0.938	0.988	0.100	0.212	0.113	0.212	0.013	0.100	0.966	0.358

Supplementary Table 3: Source-space statistics for the PC+1 condition across multiverse pipelines. Multiverse source analysis of sources in the PC+1 condition averaged over the time window with most prominent HEP difference (130 ms to 200 ms). AVG and AVG-SF were compared to aggregate the dipole sources into single ROIs. Cell background shading indicates statistical significance: light grey cells reach the significance threshold ($p < 0.05$, FDR-corrected). The p-value is printed in green when the comparison condition shows greater absolute source activity (|PC+1| > |PC-3|) and in red when it shows smaller absolute source activity (|PC+1| < |PC-3|).

		p-value: paired t-test of |PC+1| vs |PC-3| within each source									
Regularisation Parameter	Aggregation Method	Left Cingulate Gyrus posterior division	Right Cingulate Gyrus posterior division	Left Postcentral Gyrus	Right Postcentral Gyrus	Left Frontal Orbital Cortex	Right Frontal Orbital Cortex	Left Insular Cortex	Right Insular Cortex	Left Cingulate Gyrus anterior division	Right Cingulate Gyrus anterior division
0.5	AVG	0.840	0.716	0.235	0.056	<0.001	<0.001	0.958	0.117	<0.001	0.001
0.5	AVG-SF	0.540	0.126	<0.001	<0.001	0.006	0.006	0.831	0.041	<0.001	0.001
0.05	AVG	0.542	0.580	0.606	0.542	0.008	0.012	0.535	0.028	<0.001	0.006
0.05	AVG-SF	0.665	0.603	<0.001	<0.001	0.009	0.048	0.366	0.009	<0.001	0.003
0.001	AVG	0.497	0.421	0.766	0.766	0.024	0.024	0.177	0.018	<0.001	0.013
0.001	AVG-SF	0.723	0.843	<0.001	<0.001	0.031	0.208	0.163	0.005	<0.001	0.005



Supplementary Fig. 4: The ACC is more active during PC+1 than during comparable time windows of the reference condition. Source-space of HEP difference between constant time window of PC+1 condition and moving time window across HEP of PC-3 condition. The ACC is significantly more active in the PC+1 condition across most comparisons ($p_{\mathrm{FDR}} < 0.05$).

Supplementary Table 4: BOLD signal decreases – FLAME 1+2 ($Z > 3.1$, GRF-corrected $p < 0.05$), full sample ($N = 11$). FLAME 1+2 mixed-effects modelling yielded eight significant clusters. The three largest were centred on the right insular cortex (peak MNI $[34, 4, -2]$; $Z = 5.18$; 2569 voxels), left insular cortex (peak MNI $[-40, 2, -4]$; $Z = 5.47$; 2184 voxels), and the ACC (peak MNI $[4, 38, 6]$; $Z = 4.92$; 1951 voxels). Additional clusters encompassed right supramarginal gyrus, left supramarginal/superior parietal cortex, right frontal pole, brainstem (peak $[8, -28, -36]$; $Z = 4.94$), and left lateral occipital/middle temporal cortex, broadly consistent with the primary randomise/TFCE results (Fig. 5, Table 2). Cluster-correction thresholds were $Z > 3.1$, GRF-corrected $p < 0.05$. Clusters are ordered by volume. Z-max: peak Z-statistic (FLAME 1+2). p: family-wise error (FWE)-corrected cluster p-value. MNI coordinates refer to MNI152 standard space (2 mm isotropic). Anatomical labels are from the Harvard-Oxford Cortical and Subcortical Structural Atlases (2 mm maximum probability atlas, 25 % threshold). ACC: anterior cingulate cortex; COG: centre of gravity; L: left; R: right; ant.: anterior division; post.: posterior division; inf.: inferior division; temporoocc.: temporooccipital part.

Cluster	Voxels	Peak MNI (x, y, z)	Z-max TFCE	p	Peak region (HO atlas)	COG region (HO atlas)
1	2569	34, 4, −2	5.18	< 0.0001	–	R Insular Cortex
2	2184	−40, 2, −4	5.47	< 0.0001	L Insular Cortex	L Insular Cortex
3	1951	4, 38, 6	4.92	< 0.0001	L/R ACC	L/R ACC
4	1093	48, −38, 58	4.92	< 0.0001	R Supramarginal Gyrus (post.)	R Supramarginal Gyrus (post.)
5	938	−40, −46, 44	5.27	< 0.0001	L Supramarginal Gyrus (post.)/Superior Parietal Lobule	L Supramarginal Gyrus (post.)
6	785	48, 42, 18	4.81	0.0001	R Frontal Pole	R Frontal Pole
7	331	8, −28, −36	4.94	0.0162	Brainstem	Brainstem
8	265	−52, −66, −4	4.56	0.0384	L Lateral Occipital Cortex (inf.)	L Middle Temporal Gyrus (temporoocc.)/Lateral Occipital Cortex (inf.)

Supplementary Table 5: BOLD signal decreases – FLAME 1 ($Z > 3.1$, GRF-corrected $p < 0.05$), full sample ($N = 11$). The most conservative parametric approach (FLAME 1) identified four significant clusters, centred on bilateral insular cortex, ACC and left supramarginal gyrus. FLAME 1 uses ordinary least-squares mixed-effects estimation without MCMC sampling and serves as the most conservative parametric check. Cluster-correction thresholds were $Z > 3.1$, GRF-corrected $p < 0.05$. Clusters are ordered by volume. For remaining abbreviations see Supplementary Table 4.

Cluster	Voxels	Peak MNI (x, y, z)	Z-max TFCE	p	Peak region (HO atlas)	COG region (HO atlas)
1	726	28, 18, −2	3.76	0.0002	R Insular Cortex	R Insular Cortex
2	374	−32, 14, −4	3.80	0.0095	L Insular Cortex	L Insular Cortex
3	349	2, 30, 16	3.92	0.0129	L/R ACC	L/R ACC
4	303	−44, −44, 46	3.74	0.0232	L Supramarginal Gyrus (post.)	L Supramarginal Gyrus (post.)

Supplementary Table 6: BOLD signal decreases – FLAME 1+2 ($Z > 3.1$, GRF-corrected $p < 0.05$), PVC-dominant subgroup ($N = 7$). In the PVC-dominant subgroup ($N = 7$), FLAME 1+2 identified six significant clusters. Compared to the full sample (Supplementary Table 4), bilateral insular and ACC deactivations showed higher peak Z-statistics, consistent with greater statistical power when restricting the sample to the dominant PC subtype. One participant with mixed PVC/PAC contributions (sub-31) was excluded from all subtype analyses. No significant clusters were identified in the PAC-dominant subgroup ($N = 3$) at the applied threshold. Note that the PAC-dominant subgroup is substantially underpowered for formal inference; a null result should not be interpreted as evidence of absence. Only PVC-dominant participants (> 95 % PVCs on 24-hour Holter ECG) were included. Cluster-correction thresholds were $Z > 3.1$, GRF-corrected $p < 0.05$. Clusters are ordered by volume. For remaining abbreviations see Supplementary Table 4.

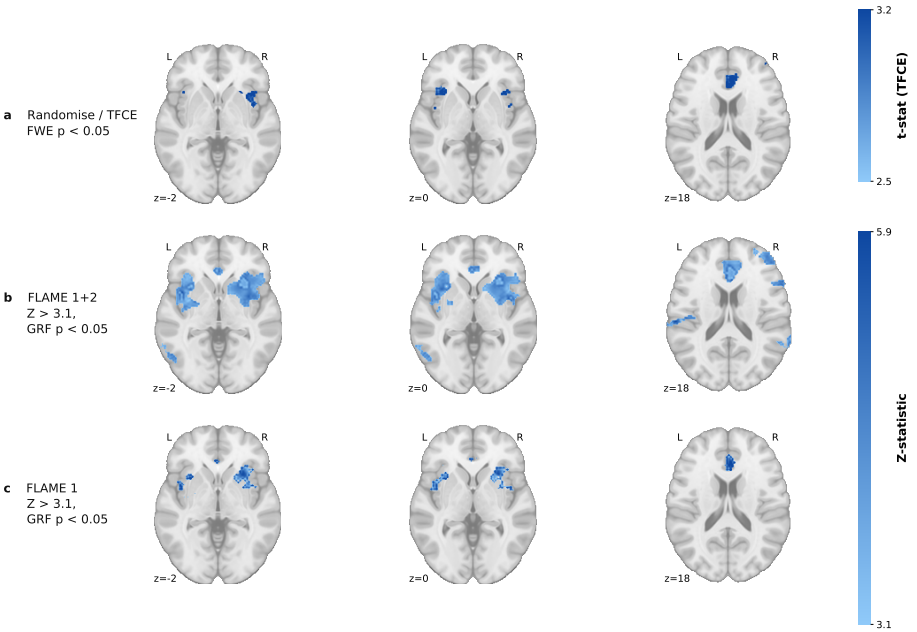
Cluster	Voxels	Peak MNI (x, y, z)	Z-max TFCE	p	Peak region (HO atlas)	COG region (HO atlas)
1	2758	−48, −22, 16	6.40	< 0.0001	L Central Opercular Cortex	L Insular Cortex
2	1976	48, −16, 12	6.38	< 0.0001	R Central Opercular Cortex/Heschl's Gyrus	R Insular Cortex
3	895	6, −26, −32	6.33	0.0001	Brainstem	Brainstem
4	562	−52, −36, 40	5.00	0.0014	L Supramarginal Gyrus (ant.)	L Supramarginal Gyrus (post.)
5	538	2, 32, 16	5.77	0.0018	L/R ACC	L/R ACC
6	399	−6, 22, 40	5.04	0.0085	L Paracingulate Gyrus	R Paracingulate Gyrus

Supplementary Table 7: Inter-beat intervals surrounding premature ventricular contractions. IBIs of the heartbeats in the PVC condition.

	IBI in ms		
	Sinus beat	**PVC-1 to PVC**	**PVC to PVC+1**
mean	930.69	564.54	1247.22
SD	115.26	88.62	211.48
min	597.20	451.38	683.56
max	1217.97	891.00	1579.00

Supplementary Table 8: Inter-beat intervals surrounding premature atrial contractions. IBIs of the heartbeats in the PAC condition.

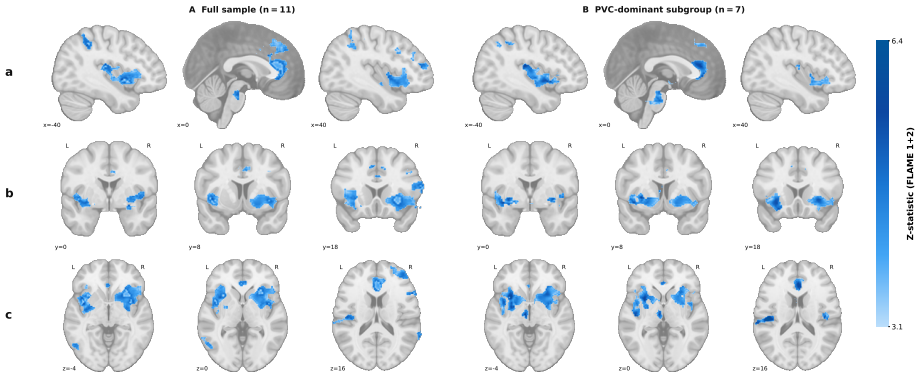
	IBI in ms		
	Sinus beat	**PAC-1 to PAC**	**PAC to PAC+1**
mean	922.32	579.87	1105.26
SD	141.24	92.17	163.40
min	585.30	436.52	701.91
max	1225.74	808.53	1441.00



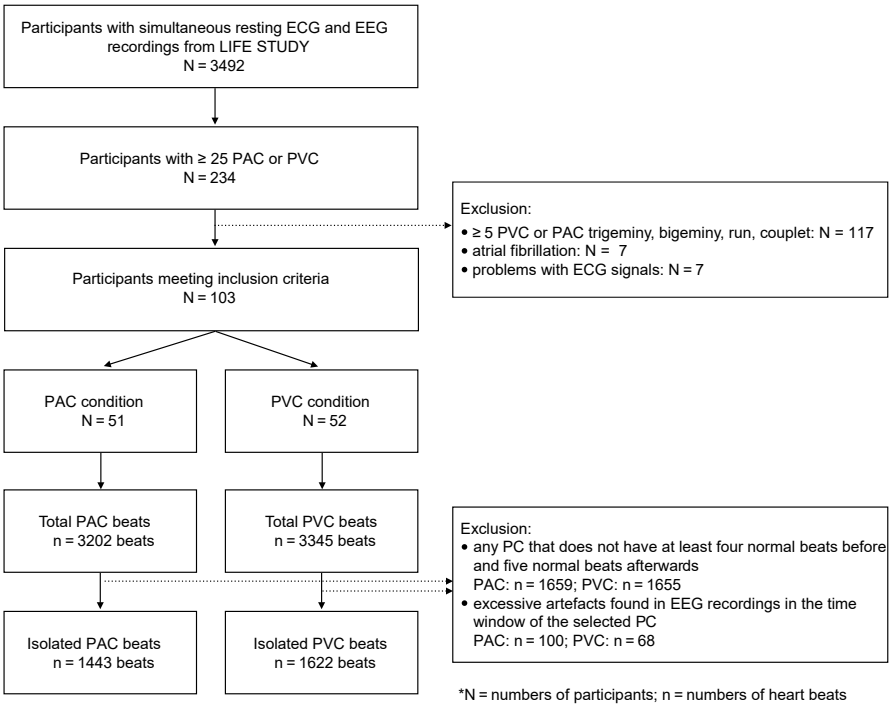
Supplementary Fig. 5: Convergence of significant deactivations across statistical models. Voxels reaching significance under each of three statistical frameworks (PCs vs regular heartbeats; $N = 11$) are shown. **(a)** Non-parametric permutation testing (randomise/TFCE, FWE-corrected $p < 0.05$). **(b)** Parametric mixed-effects modelling (FLAME 1+2, $Z > 3.1$, GRF-corrected $p < 0.05$). **(c)** The most conservative parametric model (FLAME 1, $Z > 3.1$, GRF-corrected $p < 0.05$). Each row shows the same three axial slices centred on the cluster centres of gravity of the primary ROIs. The colour scale is as in Fig. 5 (the t-statistic for row (a); the Z-statistic for rows (b) and (c)). Bilateral insular cortex and ACC reached significance across all three frameworks. L: left; R: right. Coordinates are in MNI152 standard space.

Supplementary Table 9: T-peak amplitude matching of PC+1, N, and PC-3 epochs. Matching epochs of PC+1 with epochs in the PC-3 and N conditions using the T-peak amplitude. Column 'Number of Epochs' describes the number of remaining epochs per participant after matching.

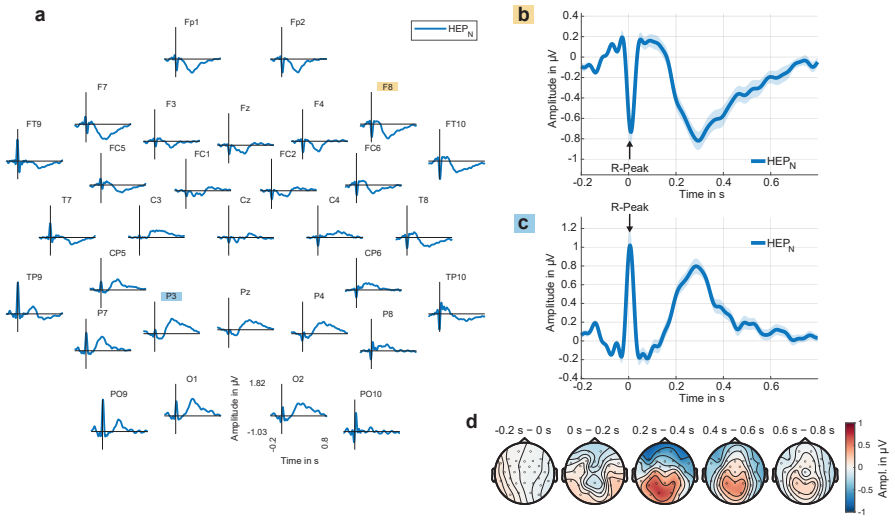
		Unmatched T-peak ampl. in µV		**Matched T-peak ampl. in µV**	
	Number of Epochs	**PC-3 and N**	**PC+1**	**PC-3 and N**	**PC+1**
mean	29.10	166.81	159.38	159.79	159.18
SD	14.71	74.06	69.10	69.30	69.17
min	8.00	38.73	28.95	29.08	28.95
max	88.00	378.97	369.10	369.13	369.10



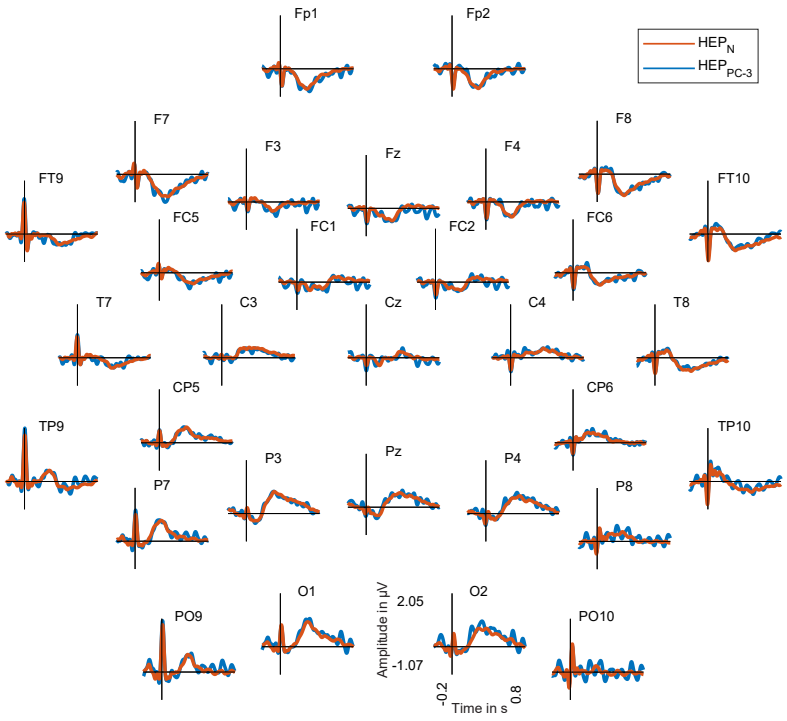
Supplementary Fig. 6: Insular-ACC deactivation is preserved and amplified in the PVC-dominant subgroup. Whole-brain BOLD signal decrease maps are shown for the full sample ($N = 11$; left) and the PVC-dominant subgroup ($N = 7$; right). Both maps show FLAME 1+2 Z-statistic results ($Z > 3.1$, GRF-corrected $p < 0.05$), displayed on identical slices with matched colour scales. Cluster centres of gravity served as slice coordinates (sagittal, coronal, and axial rows). L: left; R: right. Coordinates are in MNI152 standard space. In the PVC-dominant subgroup, bilateral insular and ACC deactivations are spatially more extensive and show higher peak Z-statistics, consistent with greater signal-to-noise when the sample is restricted to the dominant PC subtype.



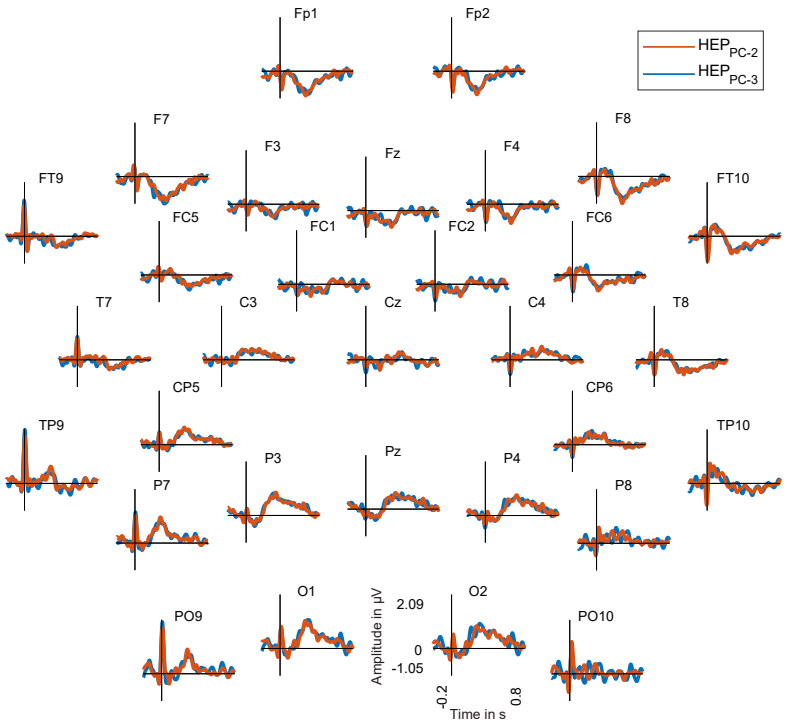
Supplementary Fig. 7: Participant selection flow chart. Flow chart of the selection of participants with PC beats.



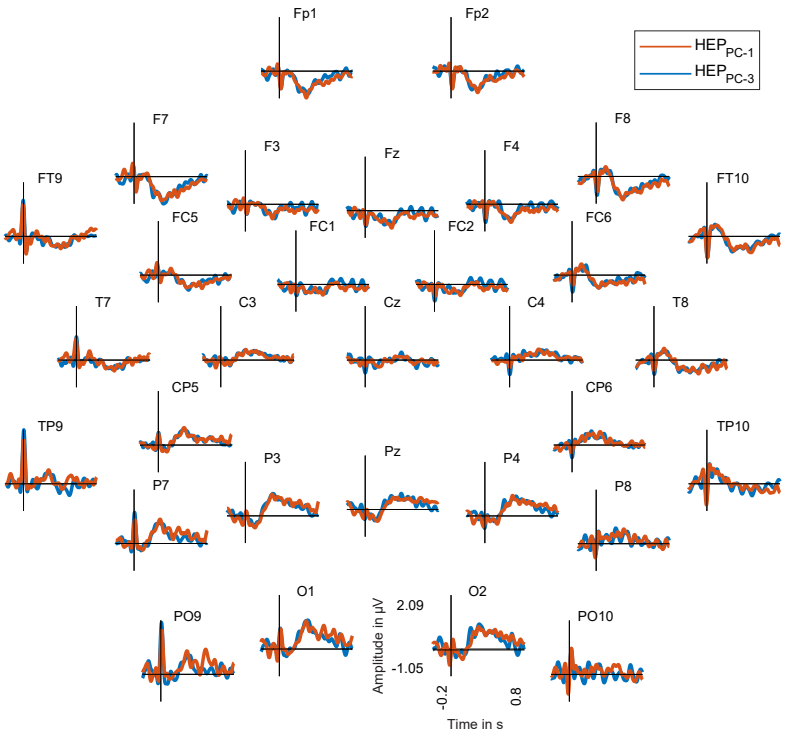
Supplementary Fig. 8: Grand average heartbeat-evoked potential of regular sinus beats. HEP of sinus beats (N). Grand average over all participants. **(a)** HEP in each EEG channel. **(b)** HEP in electrode F8. The colour-shaded regions around the lines mark the ±1 SEM. **(c)** HEP in electrode P3. The colour-shaded regions around the lines mark the ±1 SEM. **(d)** Topographies over time.



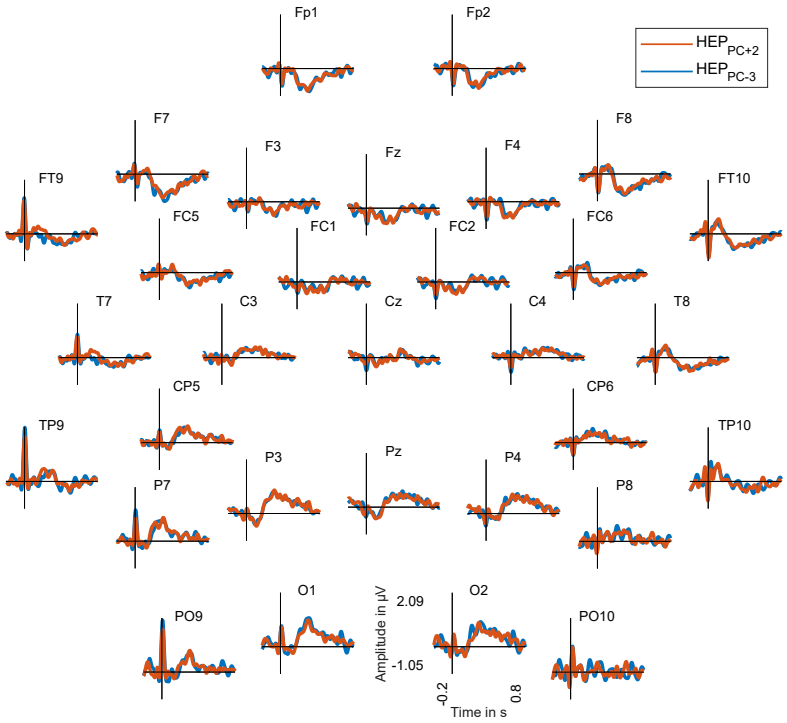
Supplementary Fig. 9: PC-3 does not significantly differ from regular sinus beats, confirming its suitability as the reference condition. No significant differences ($p > 0.3$) in HEP in the time domain between conditions PC-3 and N (number of epochs in N condition not downsampled).



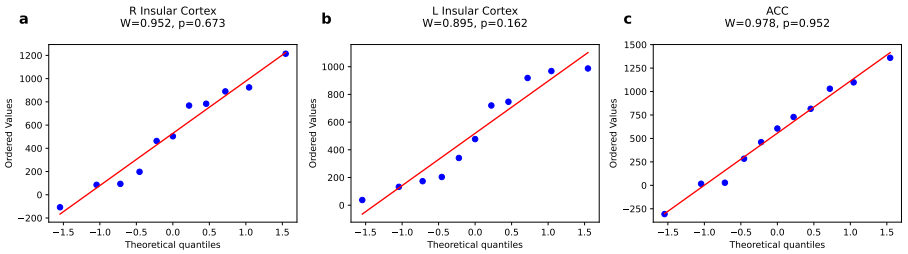
Supplementary Fig. 10: PC-2 does not significantly differ from the reference condition. No significant differences ($p > 0.7$) in HEP in the time domain between conditions PC-2 and PC-3.



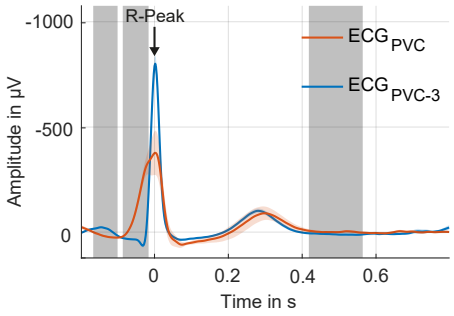
Supplementary Fig. 11: PC-1 does not significantly differ from the reference condition. No significant differences ($p > 0.3$) in HEP in the time domain between conditions PC-1 and PC-3.



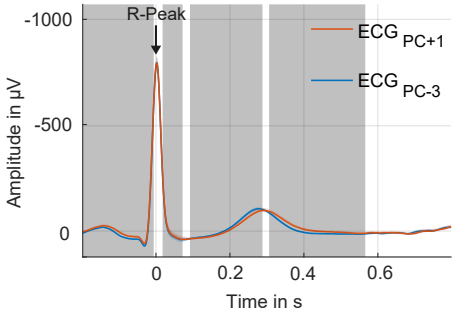
Supplementary Fig. 12: Return to normal neural activity after post-textrasystolic beat. No significant differences ($p > 0.7$) in HEP in the time domain between conditions PC+2 and PC-3.



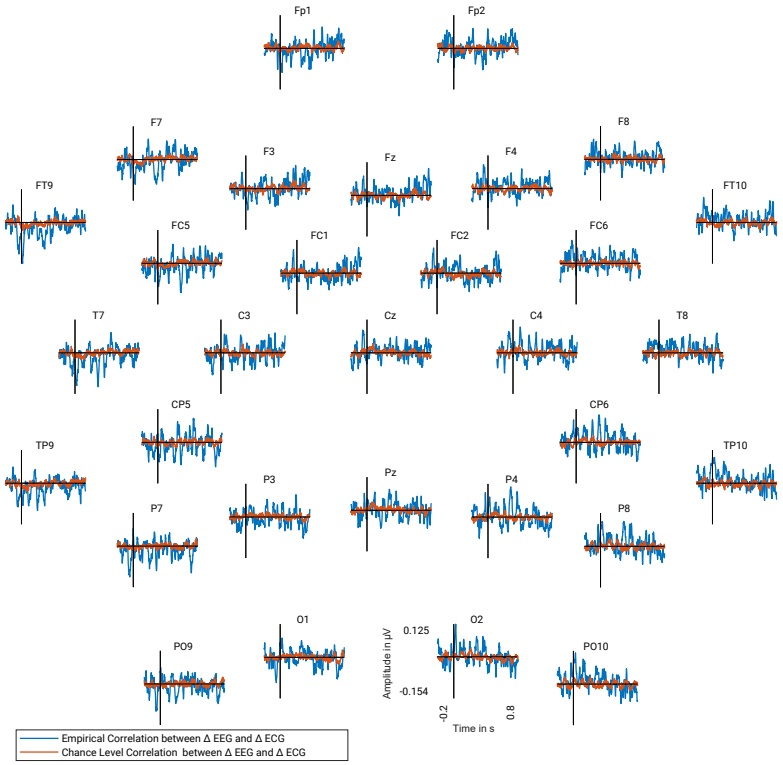
Supplementary Fig. 13: Normality of first-level contrast estimates at primary regions of interest. Quantile-quantile (Q-Q) plots of first-level contrast estimates (PCs < regular heartbeats) are shown across $N = 11$ participants, averaged within three results-independent Harvard-Oxford probabilistic atlas masks ($\geq 25\,\%$ probability threshold): **(a)** right insular cortex (Shapiro-Wilk $W = 0.952$, $p = 0.673$); **(b)** left insular cortex (Shapiro-Wilk $W = 0.895$, $p = 0.162$); **(c)** ACC (Shapiro-Wilk $W = 0.978$, $p = 0.952$). This indicates no violation of normality at the primary ROIs (Supplementary information A.8). Note that the primary inference is based on non-parametric permutation testing (randomise/TFCE), which requires no distributional assumptions given the small sample size ($N = 11$).



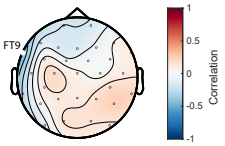
Supplementary Fig. 14: Main difference between the ECG of the premature ventricular contractions and the reference condition is during a different time window than the neural finding. ECG of PVC and reference condition (Monte Carlo $p < 0.0144$). The grey-shaded areas highlight the time window during which the most pronounced differences occur. The colour-shaded areas around the lines mark the ±1 SEM. Grand average over all participants ($N = 52$).



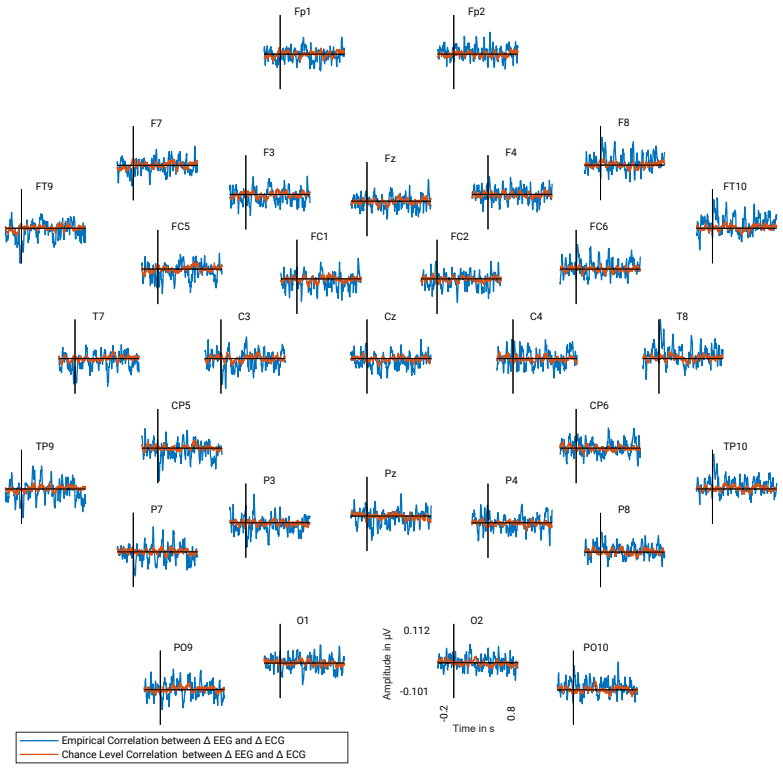
Supplementary Fig. 15: ECG of the postextrasystolic beat appears later and less pronounced than the reference. ECG of PC+1 and reference condition (Monte Carlo $p < 0.023$). The grey-shaded areas highlight the time window during which the most pronounced differences occur. The colour-shaded areas around the lines mark the ± 1 SEM. Grand average over all participants ($N = 103$).



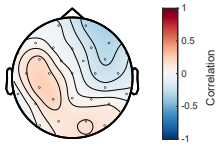
Supplementary Fig. 16: Differences in the ECG do not influence the EEG differences in the PVC condition. Time course of the empirical and chance level Fisher-transformed correlation between differences in the ECG and EEG for the PVC with no significant findings.



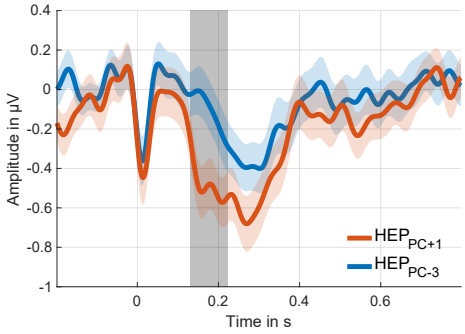
Supplementary Fig. 17: ECG-EEG correlation during the PVC time window of interest shows only significant effect at electrode FT9. Channelwise correlation between differences in the ECG and EEG over the averaged time window of 220 ms to 350 ms for the PVC with a significant finding in electrode FT9 ($\rho = -0.49; p_{\mathrm{FDR}} < 0.05$, minimal correlation: -0.49, maximal correlation: 0.24).



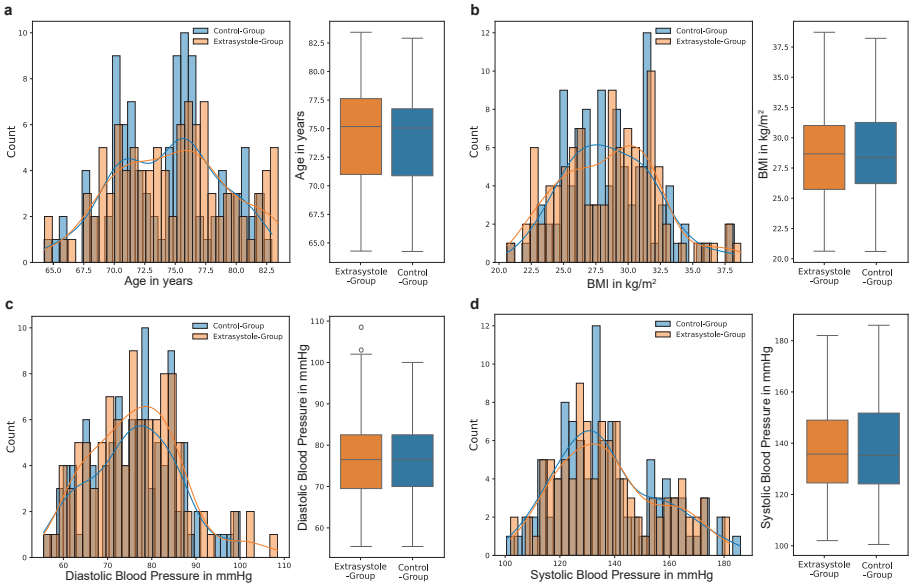
Supplementary Fig. 18: Differences in the ECG do not influence the EEG differences in the PC+1 condition. Time course of the empirical and chance level Fisher-transformed correlation between differences in the ECG and EEG for the PC+1 with no significant findings.



Supplementary Fig. 19: No channelwise ECG-EEG correlation during the PC+1 time window of interest. Channelwise correlation between differences in the ECG and EEG over the averaged time window from 130 ms to 200 ms for the PC+1 with no significant finding ($p_{\mathrm{FDR}} > 0.05$, minimal correlation: -0.3, maximal correlation: 0.24).



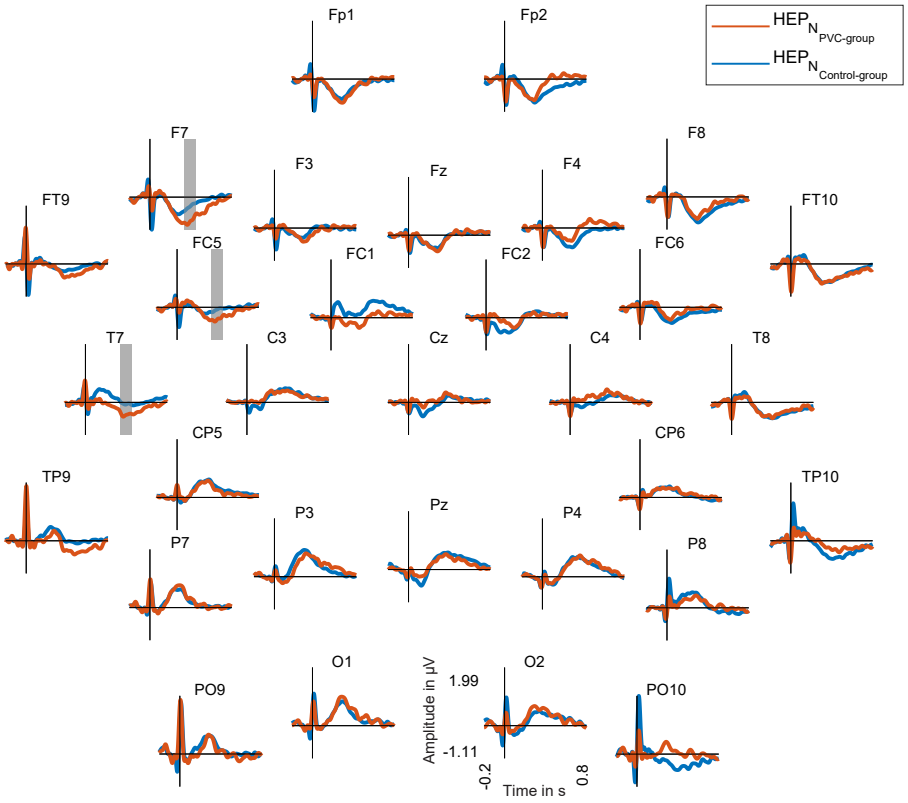
Supplementary Fig. 20: The PC+1 neural difference persists after T-peak amplitude matching. Comparison between PC+1-condition and reference condition based on matched epochs using their T-peak amplitudes. Negative cluster over central-frontal electrodes (Monte Carlo $p < 0.002$). The grey-shaded area highlights the time window of the found cluster. The colour-shaded areas around the lines mark the ±1 SEM.



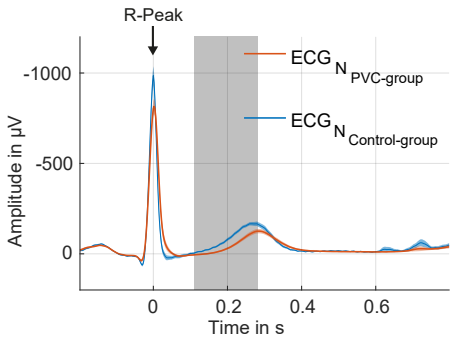
Supplementary Fig. 21: Physiological matching between premature contraction participants and controls. **(a)** Age, **(b)** BMI, **(c)** diastolic blood pressure and **(d)** systolic blood pressure distribution of the premature contractions and the matched control group.

Supplementary List 1: Inclusion and exclusion criteria for the matched control group. Inclusion and exclusion criteria that needed to be met by the control group.

- no pathological ECG events detected by CER-S, such as:
  - Atrial Fibrillation
  - Atrial Flutter
  - Atrial Tachycardia
  - Atrioventricular Block
  - Bradycardia
  - Isolated Supraventricular Beat (PAC)
  - Isolated Ventricular Beat (PVC)
  - Pause
  - Prolonged RR Interval
  - Supraventricular Bigeminy
  - Supraventricular Couplet
  - Supraventricular Run
  - Supraventricular Tachycardia
  - Supraventricular Trigeminy
  - Torsade de Pointes
  - Ventricular Bigeminy
  - Ventricular Couplet
  - Ventricular Fibrillation
  - Ventricular Flutter
  - Ventricular Run
  - Ventricular Tachycardia
  - Ventricular Trigeminy
- no pacemaker, as reported by LIFE
- a sinus rhythm, as reported by LIFE



Supplementary Fig. 22: Sinus-beat evoked activity differs within a small cluster between PVC participants and matched controls. Comparison between the PVC participants and the matched control group for the N-condition. Negative cluster over F7, FC5 and T7 electrodes (Monte Carlo $p < 0.03$). The grey-shaded area highlights the time window of the found cluster.



Supplementary Fig. 23: Sinus-beat ECG differs between PVC participants and matched controls with most prominent difference within a different time window than the neural difference. Comparison between the PVC participants and the matched control group for the N-condition. Cluster between 110 ms to 280 ms (Monte Carlo $p < 0.0004$). The grey-shaded area highlights the time window of the found cluster. The colour-shaded areas around the lines mark the ±1 SEM.